

Improving the Efficiency of Organic Solar Cells Through the Addition of Silver Nanoparticles and Cadmium Oxide

By

Matthew Brady Hunt

A thesis submitted to the Department of Physics and Physical Oceanography
in partial fulfillment of the requirements for the degree of
Master of Science

In

The Department of Physics and Physical Oceanography
Faculty of Science
Memorial University of Newfoundland

August, 2016

St. John's

Newfoundland Labrador

Abstract

The development of renewable energy technologies has received significant attention in recent years. Among the many different approaches, organic solar cells have much promise due to their low cost of manufacturing (as compared to silicon based solar cells), increased flexibility, low weight, and high cell transparency. In this study we investigate the possibility of performance enhancement of organic solar cells by the addition of silver nanoparticles as well as cadmium oxide. The effects on the performance of organic solar cells with the addition of silver nanoparticles was examined through the addition of 5, 10, 20, and 30 nm diameter silver nanoparticles within the structure of poly(3-hexylthiophene) (P3HT) and [6,6]-phenyl C₆₀ butyric acid methyl ester (PCBM) based devices. It was found that in general the addition of silver nanoparticles improved the overall performance of the devices with the 5 and 10 nm nanoparticles providing the greatest improvement in performance. Additionally, cadmium oxide was tested as a buffer layer for the organic solar cells, replacing the poly(3,4-ethylenedioxythiophene) polystyrene sulfonate (PEDOT:PSS) that is normally used in organic solar cells.

To my parents, Kim and Rodger

Acknowledgements

I would like to thank Dr. Qiying Chen for his help, guidance, and supervision throughout this project, without him this project never would have been possible. I would also like to thank Dr. Liqiu Men for the help and assistance she provided throughout the experimentation process. I must also thank Dr. Todd Andrews for suggesting that I speak with Dr. Chen when I was looking for a supervisor for this project.

Next, I'd like to thank all my friends who helped keep this entire experience fun and enjoyable. Finally and perhaps most importantly I would like to thank my parents, Kim and Rodger, for their encouragement and support throughout this project. Without them, none of this would ever have been possible.

Contents

Abstract	i
Acknowledgements	iii
Contents	iv
List of Abbreviations	vii
List of Tables	ix
List of Figures	x
1 Introduction	1
1.1 Motivation	1
1.2 Photovoltaics as a Technology for Renewable Energy	2
1.3 Function and Characterization of Solar Cells	4
1.4 Performance Comparison and Potential of Solar Cells	6
1.5 Outline	7
2 The Theory Behind Organic Solar Cells	9

2.1	Basic Structure	10
2.2	Mechanisms	12
2.2.1	Exciton Generation	13
2.2.2	Exciton Diffusion	14
2.2.3	Exciton Dissociation	14
2.2.4	Charge Transport	14
2.3	Progress in Organic Solar Cells	15
2.4	Nanoparticle Doping for Performance Enhancement of Organic Solar Cells	16
2.5	Transition Metal Oxides as a Buffer Layer in Organic Solar Cells	19
3	Experimental Details	20
3.1	Introduction	20
3.2	Sample Preparation	22
3.2.1	Control Samples	27
3.2.2	Silver Nanoparticle Cells	30
3.2.3	Transition Metal Oxide Cells	33
3.2.4	Nanoparticle and Transition Metal Oxide Cells	35
3.3	Testing	36
4	Results and Discussion	39
4.1	Control Cells	41
4.2	Incorporation of Silver Nanoparticles into Organic Solar Cells	43
4.2.1	ITO/Ag-NP/PEDOT:PSS/P3HT:PCBM/Al Cells	43
4.2.2	ITO/PEDOT:PSS/P3HT:PCBM:Ag-NP/Al Cells	49

4.2.3	ITO/PEDOT:PSS/Ag-NP/P3HT:PCBM/Al Cells	55
4.2.4	ITO/PEDOT:PSS:Ag-NP/P3HT:PCBM/Al Cells	62
4.3	Incorporation of Transition Metal Oxides into Organic Solar Cells	68
4.3.1	ITO/CdO/P3HT:PCBM/Al Cells	68
4.3.2	ITO/TiO ₂ /P3HT:PCBM/CdO/Al and ITO/TiO ₂ /P3HT:PCBM/MoO ₃ /Al Cells	70
5	Conclusion	73
5.1	Summary	73
5.1.1	Silver Nanoparticle Cells	74
5.1.2	Cadmium Oxide Cells	75
5.2	Future Work	76

List of Abbreviations

Ag-NP	Silver nanoparticles
Al	Aluminum
BHJ	Bulk heterojunction
CdO	Cadmium oxide
DMSO	Dimethyl sulphoxide
FF	Fill factor
HOMO	Highest occupied molecular orbital
ITO	Indium tin oxide
J_{Max}	Current density at the maximum power point
J_{SC}	Short circuit current density
LUMO	Lowest unoccupied molecular orbital
LSPR	Localized surface plasmon resonance
MoO₃	Molybdenum trioxide
OSC	Organic solar cell
P3HT	Poly(3-hexylthiophene)
PCBM	[6,6]-phenyl C ₆₀ butyric acid methyl ester

PCE	Power conversion efficiency
PEDOT:PSS	Poly(3,4-ethylenedioxythiophene) polystyrene sulfonate
SPP	Surface plasmon polaritons
TiO₂	Titanium dioxide
TMO	Transition metal oxide
V_{Max}	Voltage at the maximum power point
V_{OC}	Open circuit voltage

List of Tables

4.1	Table of results for ITO/Ag-NP/PEDOT:PSS/P3HT:PCBM/Al cells.	48
4.2	Table of results for ITO/PEDOT:PSS/P3HT:PCBM:Ag-NP/Al cells.	54
4.3	Table of results for ITO/PEDOT:PSS/Ag-NP/P3HT:PCBM/Al cells.	61
4.4	Table of results for ITO/PEDOT:PSS:Ag-NP/P3HT:PCBM/Al cells.	67
4.5	Table of results for ITO/CdO/P3HT:PCBM/Al cells.	71

List of Figures

1.1	A picture of a solar farm taken from a high speed train in China.	3
2.1	Basic depiction of the structure of a solar cell.	10
3.1	Schematic diagram of photolithographic etching of ITO coated substrates.	23
3.2	Homemade substrate holder and shadow mask.	25
3.3	Mercury lamp and substrate (in holder with shadow mask) during UV exposure portion of the photolithographic process.	26
3.4	Structure diagram of control cells.	27
3.5	Shadow mask used for the thermal evaporation of the Al cathode.	29
3.6	Structure diagram of ITO/Ag-NP/PEDOT:PSS/P3HT:PCBM/Al cells.	30
3.7	Structure diagram of ITO/PEDOT:PSS/P3HT:PCBM:Ag-NP/Al cells.	31
3.8	Structure diagram of ITO/PEDOT:PSS/Ag-NP/P3HT:PCBM/Al cells.	32
3.9	Structure diagram of ITO/PEDOT:PSS:Ag-NP/P3HT:PCBM/Al cells.	32
3.10	Structure diagram of ITO/CdO/P3HT:PCBM/Al cells.	34
3.11	Structure diagram of ITO/TiO ₂ /P3HT:PCBM/CdO/Al cells.	34
3.12	Structure diagram of ITO/TiO ₂ /PCBM:P3HT/MoO ₃ /Al cells.	35
3.13	AM 1.5G solar simulator used during the testing of cell efficiency.	36

3.14	Computer and Keithley 2420 source meter (under the keyboard) used for testing cell efficiency.	37
4.1	J-V curve demonstrating the calculation of V_{OC} (A), V_{Max} (B), J_{Max} (C), and J_{SC} (D).	40
4.2	J-V curve for control samples, with structure of ITO/PEDOT:PSS/P3HT:PCBM/Al.	42
4.3	J-V curve for 5 nm samples, with structure of ITO/Ag-NP/PEDOT:PSS/P3HT:PCBM/Al.	44
4.4	J-V curve for 10 nm samples, with structure of ITO/Ag-NP/PEDOT:PSS/P3HT:PCBM/Al.	45
4.5	J-V curve for 20 nm samples, with structure of ITO/Ag-NP/PEDOT:PSS/P3HT:PCBM/Al.	46
4.6	J-V curve for 30 nm samples, with structure of ITO/Ag-NP/PEDOT:PSS/P3HT:PCBM/Al.	47
4.7	J-V curve for 5 nm samples, with structure of ITO/PEDOT:PSS/P3HT:PCBM:Ag-NP/Al.	50
4.8	J-V curve for 10 nm samples, with structure of ITO/PEDOT:PSS/P3HT:PCBM:Ag-NP/Al.	51
4.9	J-V curve for 20 nm samples, with structure of ITO/PEDOT:PSS/P3HT:PCBM:Ag-NP/Al.	52
4.10	J-V curve for 30 nm samples, with structure of ITO/PEDOT:PSS/P3HT:PCBM:Ag-NP/Al.	53
4.11	J-V curve for 5 nm samples, with structure of ITO/PEDOT:PSS/Ag-NP/P3HT:PCBM/Al.	56

4.12 J-V curve for 10 nm samples, with structure of ITO/PEDOT:PSS/Ag-NP/P3HT:PCBM/Al.	57
4.13 J-V curve for 20 nm samples, with structure of ITO/PEDOT:PSS/Ag-NP/P3HT:PCBM/Al.	58
4.14 J-V curve for 30 nm samples, with structure of ITO/PEDOT:PSS/Ag-NP/P3HT:PCBM/Al.	59
4.15 J-V curve for 5 nm samples, with structure of ITO/PEDOT:PSS:Ag-NP/P3HT:PCBM/Al.	63
4.16 J-V curve for 10 nm samples, with structure of ITO/PEDOT:PSS:Ag-NP/P3HT:PCBM/Al.	64
4.17 J-V curve for 20 nm samples, with structure of ITO/PEDOT:PSS:Ag-NP/P3HT:PCBM/Al.	65
4.18 J-V curve for 30 nm samples, with structure of ITO/PEDOT:PSS:Ag-NP/P3HT:PCBM/Al.	66
4.19 J-V curve for CdO samples spin coated at 3500 rpm, with structure of ITO/CdO/P3HT:PCBM/Al.	69

Chapter 1

Introduction

1.1 Motivation

Solar light and energy is the earth's only inexhaustible energy source, it is also the most important source of regenerative energy. The average annual energy input upon the earth through solar irradiation (comprised of 5% ultraviolet, 43% visible, and 52% infrared) exceeds the earth's yearly energy consumption by several thousand times [1].

Currently fossil fuels account for approximately 82% of the global energy supply, however it has recently been predicted that there will be an inevitable permanent decline in the global oil production rate within roughly the next 10 years [2, 3]. As energy consumption continues to grow world wide this decline in production will lead to the gradual deterioration of energy availability as well as the inevitable increase in energy costs.

Additionally, the burning of fossil fuels has been shown to dramatically increase the CO₂ concentration in the atmosphere. The resulting concentration increase has considerably increased the greenhouse effect on earth and at the current CO₂ emission

rate this could cause the global mean surface temperature to rise by an additional 0.6-7.0°C by 2100 [4]. This temperature increase would then be combined with the 0.3-6.0°C temperature increase as well as the 10 - 25 cm rise in global sea level since the late 1800s, both of which are most likely due to human activities [4].

The consequences of such an increase in sea level and global surface temperature could have devastating consequences on not only humans, but on other life forms as well. In fact the recent extinction of the Bramble Cay melomys also known as the Bramble Cay mosaic-tailed rat (*Melomys rubicola*), has been directly linked to human driven climate change [5].

1.2 Photovoltaics as a Technology for Renewable Energy

It is therefore apparent that new efficient and environmentally friendly power generation techniques are needed. As a result, there has been increased interest in producing energy and electricity using renewable resources such as wind, solar, and hydro. Given that solar irradiation provides several thousand times the amount of energy that we require globally [1], there has been significant focus placed upon harnessing solar energy and converting it into electricity. This increased interest has led to the development of solar cell technology in an attempt to convert unused solar radiation into electrical energy.

Silicon based solar cells have thus far been the most efficient and effective at converting solar energy into electricity. As a result, current generation solar energy farms, such as the one demonstrated in Figure 1.1, primarily consist of silicon based solar cells. Unfortunately however the electricity generated via silicon cells is very



Figure 1.1: A picture of a solar farm taken from a high speed train in China.

expensive due to the high cost of manufacturing and the associated costs have resulted in a long energy pay back time [6].

Therefore, there has been increased interest in organic solar cells (OSC) due to their low cost of manufacturing (as compared to silicon based solar cells), increased flexibility, lower weight, and improved cell transparency [7]. Such devices would provide new possibilities for power generating devices, with one such example being power generating windows.

Additionally the manufacture of silicon based photovoltaic cells is dependent upon the use of millions of gallons of water, as well as temperatures in the 300-500°C range. Moreover the fabrication of silicon based cells requires the use of large amounts of solvents, some of which are highly toxic. On the other hand many OSCs can be prepared at temperatures of 150°C or less, and while solvents are often used during production it is possible to create significantly large numbers of OSCs with just one litre of organic solvent [8].

Therefore not only do OSCs use a considerably lower amount of solvents and toxic chemicals during their fabrication, they also require less energy during their fabrication process due to the lower temperature requirements. These two factors combine to make OSCs considerably less harmful to the environment than their silicon based counterparts.

1.3 Function and Characterization of Solar Cells

Solar cells (often referred to as photovoltaic cells) convert light or solar energy into electricity using the Photovoltaic Effect. The Photovoltaic Effect is the phenomenon by which direct electrical power (measured in watts (W)) is generated from functional materials upon illumination by photons. Basically, it is the process by which two

materials in close contact can produce an electrical current or voltage from incident light or other radiant energy [9].

These two materials form what is referred to as the active layer of the solar cell whereby when struck with incident light one material acts as an electron donor and the other as an electron acceptor. When sandwiched between an anode and a cathode a current can be produced thereby outputting electrical energy from input solar energy.

Since the high conductivity in iodine-doped oxidized polypyrrole was first reported in 1963 by McNeill *et al.* [10], significant effort has been devoted to studying the electronic properties of organic semiconducting materials. This research, combined with a desire to create environmentally friendly power generation techniques has led to the development of numerous donor-acceptor systems using materials such as poly(3-hexylthiophene) (P3HT), poly[2-methoxy, 5 ethyl(2' hexyloxy) paraphenylenevinylene] (MEH-PPV), and [6,6]-phenyl C₆₀ butyric acid methyl ester (PCBM).

For this work P3HT was chosen as a donor due to its high hole mobility, extended absorption in the red spectral region (up to 650 nm), and its high environmental stability [11]. PCBM was chosen as the acceptor due to its favorable solubility and absorption profiles, additionally PCBM is a derivative of fullerene (C₆₀) and thus possesses high electron affinity, furthermore C₆₀ and its derivatives absorb at wavelengths shorter than 400 nm as well as in infrared to visible regions [12, 13].

Interestingly enough, in the year 2000, the Nobel prize for Chemistry was awarded to H. Shirakawa, A. J. Heeger, and A. G. MacDiarmid for the discovery and development of conductive polymers [14].

1.4 Performance Comparison and Potential of Solar Cells

The percentage of absorbed light that is converted into electrical energy is known as the power conversion efficiency (PCE), and the PCE is the single most important standard parameter used when evaluating the performance of solar cells. Presently solar cells comprised of inorganic materials such as silicon offer roughly 3-4 times the efficiency of their organic counterparts. In fact, inorganic solar cells often offer a PCE in excess of 30% [15], and results as high as 46% have been reported [16]. Organic solar cells on the other hand have only recently begun to show PCEs in excess of 10% [17, 18].

Therefore there are numerous improvements required in both efficiency and stability in order for OSCs to become competitive with the performance of inorganic solar cells. In order to accomplish the required improvements it is imperative that active layer materials with the best donor-acceptor properties are chosen or that additional materials that improve these properties are added to the active layer.

Additionally it is vitally important that there is excellent conductivity between the active layer and the anode and cathode. One such method of improving the conductivity is the addition of a buffer material which will more easily allow an electron to move from the active layer to the anode or cathode. In order to ensure that the active layer receives the maximum amount of light exposure possible, it is also important that the optical properties of any added material are accounted for. Accounting for these properties will help guarantee the maximum possible light transmission to the active layer.

1.5 Outline

There are two major limitations that must be overcome before OSCs are able to find practical applications. These limitations are the efficiency and the stability of the cells, and the goal of this project will be to improve the efficiency of the devices through the addition of silver nanoparticles into the structure of the OSCs and through the application of cadmium oxide within the devices.

With the exception of the vacuum deposition of an aluminum (Al) film as a cathode, all other steps of fabrication and characterization in this work has been undertaken in ambient atmosphere.

Preliminary work began with a literature review focused primarily upon the mechanics of OSCs and the numerous methods for improving the performance of the devices. The focus of this review then shifted to examining the use of nanoparticles in OSCs and how their use can improve device performance. Continuing from this point, an examination of the use of transition metal oxides (TMO) in OSCs was completed.

As is discussed in Chapter 2, the results of the literature review showed that while the use of gold nanoparticles in OSCs has been studied fairly extensively [19, 20, 21, 22, 23], the use of silver nanoparticles (Ag-NP) in OSCs has only seen a moderate amount of study [24, 25]. As part of this work it was therefore decided to test the effects that different sizes of Ag-NPs would have on device performance, and for these tests Ag-NPs with diameters of 5 ± 2 , 10 ± 2 , 20 ± 3 , and 30 ± 3 nm were chosen.

Furthermore the review of the use of TMOs in OSCs showed that despite cadmium oxide's (CdO) positive transmission and conductivity properties, it has seen minimal study for use in OSCs. This lack of study is likely the result of cadmium's toxicity and its associated hazards to human health. These hazards include but are not limited

to lung edema, kidney damage, low grade of bone mineralization, increased rate of osteoporosis, and intense bone associated pain [26]. As a result, it was decided to take the necessary safety precautions and then test the effectiveness and performance of CdO in an OSC.

The experimental procedures and performance measuring methods are laid out in Chapter 3. Included in the chapter is the exact fabrication process for the ITO/PEDOT:PSS/P3HT:PCBM/Al, ITO/Ag-NP/PEDOT:PSS/P3HT:PCBM/Al, ITO/PEDOT:PSS/P3HT:PCBM:Ag-NP/Al, ITO/PEDOT:PSS/Ag-NP/P3HT:PCBM/Al, ITO/PEDOT:PSS:Ag-NP/P3HT:PCBM/Al, ITO/CdO/PCBM:P3HT/Al, ITO/TiO₂/PCBM:P3HT/CdO/Al, and ITO/TiO₂/P3HT:PCBM/MoO₃/Al cell structures which were tested.

The properties and performance of each cell structure are documented and discussed in Chapter 4. Within this chapter the nanoparticle size with the highest efficiency in each of the related structures is identified and discussed. Additionally the potential use of CdO as a buffer layer for OSCs is examined.

Furthermore, in Chapter 5 an overview and summary of the successful experiments is given and the potential applications of the successful devices is discussed. Finally the potential for future work is commented upon and potential approaches are discussed.

Chapter 2

The Theory Behind Organic Solar Cells

Solar cells, also known as photovoltaic cells, are devices that convert the energy from light into electricity. This conversion occurs through the photovoltaic effect which is the process in which two materials in close contact can produce an electrical current/voltage from incident light or other radiant energy [9].

The photovoltaic effect was first demonstrated by Edmond Becquerel in 1839, and has previously been referred to as the Becquerel Effect [27]. In 1883 Charles Fritts used this theory to build the first solid state solar cell, achieving an efficiency of $\sim 1\%$ [28, 29]. Vast improvements in solar cell technology have occurred since that time and an efficiency of 46% has been reported by Soitec and CEA-Leti, France, together with the Fraunhofer Institute for Solar Energy Systems ISE, Germany [16].

The first reported OSC was in 1958 by Kearns and Calvin, however the efficiency of the cells stayed in the range of 0.1% until 1985 when Tang achieved an efficiency of $\sim 1\%$ [30, 31].

2.1 Basic Structure

All solar cells, regardless of their individual chemical make up will have the same basic structure. This structure in its simplest form is shown in Figure 2.1 below, however it should be noted that under certain circumstances it is possible for the positions of the anode and cathode to be reversed.

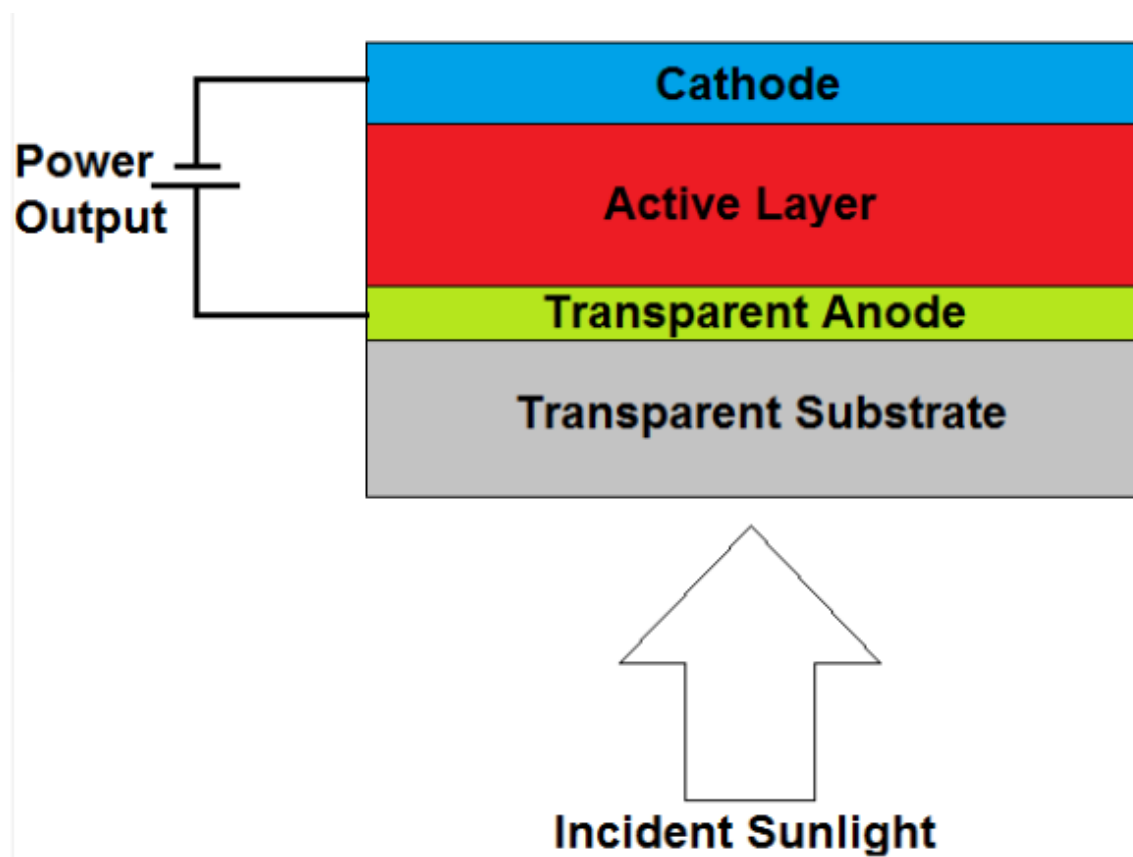


Figure 2.1: Basic depiction of the structure of a solar cell.

Solar cells can be comprised of many different layers, consisting of various components and thicknesses. In organic solar cells, the transparent substrate will generally be glass and will often be coated with Indium Tin Oxide (ITO) which decreases the surface roughness and acts as the transparent anode. Other materials such as aluminum-doped zinc oxide [32], gallium-doped zinc oxide [33], and zinc tin oxide

[34] have also been used previously as a transparent anode.

It is also common to place a layer known as an anodic buffer layer between the transparent anode and the active layer. The anodic buffer layer helps to improve conduction between the active layer and the anode, and promotes additional light absorption in the active layer. The most common material used as a buffer layer in organic solar cells is poly(3,4-ethylenedioxythiophene) polystyrene sulfonate (PEDOT:PSS), although numerous other materials have also been used successfully [35, 36, 37, 38].

The active layer can be comprised of a single layer of a mixed compound, or of multiple layers stacked on top of one another. In both instances the active layer will consist of separate materials that act as an electron donor and as an electron acceptor. Poly(3-hexylthiophene) (P3HT) and [6,6]-phenyl C₆₀ butyric acid methyl ester (PCBM) are two organic compounds that are commonly used in the production of OSCs.

A layer known as the cathodic buffer is often placed on top of the active layer in order to separate it from the cathode. This layer acts similarly to the anodic buffer in that it promotes better conductivity between the cathode and active layers, as well as promoting additional absorption. Two common materials used for this layer are a lithium-fluoride (LiF) mixture and calcium (Ca); this layer in general is considerably thinner than the cathode layer.

Finally the cathode layer is placed on top of the cathodic buffer completing the cell. The cathode is most often comprised by one of two materials, either aluminium (Al) or silver (Ag), however aluminium is the most commonly used material.

2.2 Mechanisms

The active layer of organic solar cells is comprised of organic semiconductors arranged in either a bilayer or bulk heterojunction (BHJ) structure. In a bilayer structure the donor layer is applied on top of the anode layer, and the acceptor layer is applied separately on top of the donor layer; this gives a sharp well defined interface between the two materials [39].

In a BHJ structure the acceptor and donor materials are mixed prior to application onto the anode, this gives a highly folded architecture so that all excitons (electron-hole pairs) are formed near a heterojunction interface [40]. This blended donor/acceptor architecture is a bicontinuous and interpenetrating network with nanoscale domains, thus significantly increasing the interfacial area between the donor and acceptor. As a result, each interface lies within a distance less than the exciton diffusion length ($\sim 10 - 20$ nm [41]), thus allowing more excitons to diffuse and greatly improving device performance [6]. The BHJ structure is currently the most successful device architecture for organic photovoltaics [40], and as a result will be the structure used in the experimental portion of this project.

Organic semiconductors are generally classified into two categories, small molecules or oligomers and polymers. Furthermore organic semiconductors are mainly formed from hydrocarbon compounds with a backbone of carbon atoms, and the strong bonds that form the backbone are a result of an overlap of the sp^2 hybridized atomic orbitals of adjacent carbon atoms. The result is a bonding of σ and an antibonding of σ^* orbitals. Additionally π and π^* orbitals are formed from the overlap of the remaining unhybridized p orbitals. The energies of these π orbitals are higher than those of the σ orbitals and the energies of the π^* orbitals are lower than those of the σ orbitals [6].

Additionally the resulting overlap of frontier π molecular orbitals and adjacent molecules or polymer chains represents the strength of the intermolecular electronic couplings and thus governs the charge carrier mobilities in organic semiconductors [6].

Organic solar cell materials include hole-conducting p-type semiconductors and electron conducting n-type semiconductors, as well as interfacial layer materials. Generally polymer semiconductors are dominant p-type materials due to solution process-ability and diversity of structures [30]; an alternating donor-acceptor strategy is broadly used to tune the energy levels of these polymeric semiconductors [6]. Whereas dominant n-type materials are fullerene derivatives due to their triplet degeneration of the lowest unoccupied molecular orbital (LUMO) [42], fast charge splitting [43], and good electron mobility [44].

In order to successfully convert solar energy into electricity there is a four step process that occurs in OSCs, these steps are exciton generation, exciton diffusion, exciton dissociation, and charge transport to the electrodes.

2.2.1 Exciton Generation

Exciton generation is the process by which a photon is absorbed, and an electron is excited from the highest occupied molecular orbital (HOMO) of the organic semiconductor to the LUMO of the organic semiconductor. This process leads to the formation of an electron-hole pair called an exciton, as opposed to the generation of free charge carriers in inorganic solar cells. The binding energy of this exciton is on the order of a few tenths of an electron volt (eV).

It is important to note that the band gap of the organic semiconductor determines the broadness of absorption of the solar spectrum; the smaller the band gap the

broader the spectrum of light that can be absorbed [6].

2.2.2 Exciton Diffusion

In order for the exciton to dissociate into separate positive and negative charges it must first diffuse to the donor-acceptor interface. Exciton diffusion lengths are generally around 10-20 nm for organic semiconductors, and these diffusion lengths limit the thickness of cell bi-layers and donor-acceptor (D-A) phase separation length. If the layers are too thick, the excitons can decay through radiation or non-radiative pathways and energy will be lost [6].

2.2.3 Exciton Dissociation

An electric field is required to split excitons into separate positive and negative charges. The required electric field can be external or it can be a local electric field created at the D-A interface due to significant changes in the potential energy of the donors and acceptors. The forming of heterojunction interfaces from donor conjugated materials with electron acceptors is an efficient method of splitting excitons to form separate charges.

The mechanism most often used to describe the dissociation process is a transition from the exciton state down to the lowest charge transfer state. This transition is believed to occur when the hole sits on the HOMO of a donor material and the electron on the LUMO of a neighboring acceptor molecule [6].

2.2.4 Charge Transport

In order to achieve high efficiency solar cells it is necessary for separated charges to be transported to the electrodes before they decay or recombine. The mobilities of

the donor and acceptor are therefore critical for the charge carrier transport.

A gradient of potentials of electrons and holes exists in the donor-acceptor junction, this gradient is determined by the HOMO of the donor and the LUMO of the acceptor. This internal electric field determines the maximum open circuit voltage of the cell and drives the movement of the charge carriers. An external electric field can affect the cell in the same manner as the internal field, this is formed by using asymmetrical contacts, with a low work function metal for collecting electrons and a high work function metal for collecting holes. For each of the respective charges a concentration of gradients can lead to diffusion currents.

After the charge carriers have been transported to the interface between the organic materials and the electrodes they are extracted to the electrodes. In order for efficient collection to occur, there must be an ohmic contact between the organic material and the electrode. It is therefore important to ensure the alignment of the energy levels of the materials with the work functions of the electrodes.

In a solar cell using a P3HT:PCBM active layer, the work function of the anode must align with the HOMO of P3HT, and the work function of the cathode must align with the LUMO of PCBM. It is also possible to use inter (buffer) layers between the electrodes and active layers in order to influence the interfacial charge density distributions and help align the respective energy levels [6].

2.3 Progress in Organic Solar Cells

Research into the photovoltaic effects in organic cells truly kicked off in the 1950s when several groups [45, 46] were able to measure photo-electromotive forces in various organic semiconductors on inorganic substrates. Since that time there has been significant progress in not only the development of materials for use in OSCs but also

in improving the performance and efficiency of these devices.

An example of some organic materials that have been developed for and used in OSCs are P3HT, MEH-PPV, PCBM, poly[2-methoxy-5-(3',7'-dimethyloctyloxy)-1,4-phenylenevinylene] (MDMO-PPV), and Poly(3-alkylthiophene) (P3AT) [47].

It was not until 1986 when Tang reported a 0.95% efficient thin film organic cell based upon a single donor-acceptor heterojunction that OSCs began to attract a lot of attention [39]. However it was not until the late 1990s that rapid and considerable progress began to be made [48]. Many of these advances began with developments in solution-processed polymer blend cells which resulted in efficiencies as high as 2.55% [49, 50]. Additionally developments in vacuum or vapor-phase deposited small molecule based cells resulted in efficiencies as high as 3.6% [51].

Recently there has been success in improving solar cell performance by doping metallic nanoparticles into the OSCs. As recently as 2012, such experiments have achieved efficiencies as high as 8.79% [52, 53]. Additionally in 2015 an efficiency of 11.55% was reported by Chen *et al.* and this feat was accomplished using triple-junction polymer solar cells [54].

2.4 Nanoparticle Doping for Performance

Enhancement of Organic Solar Cells

Recently there has been significant study on doping metallic nanoparticles into the various layers of organic solar cells in order to improve cell performance and efficiency. Works such as those completed by Hamdan *et al.*, Kalfagiannis *et al.*, Lee *et al.*, Kyungkon *et al.*, and Qiao *et al.* have shown improvements in power conversion efficiency (PCE) as high as 70% [21, 24, 25, 55, 56].

While gold nanoparticles have thus far given the highest increase in device performance ($\sim 70\%$), silver nanoparticles (Ag-NPs) have also been shown to give significant increases (up to $\sim 41\%$) to device performance [25, 55]. However most experiments using Ag-NPs have focused primarily on studying the effect of a single size of Ag-NP, or have used multiple sizes of Ag-NPs simultaneously. Therefore this work will focus upon the benefits generated by various sizes of silver nanoparticles, with the goal of optimizing NP sizes in various applications within OSCs.

Nanoparticle usage in OSCs is done to enhance the absorption of the cell without significantly changing the thickness of the various layers. This improvement is accomplished through plasmonics which is the properties of collective electronic excitations (known as surface plasmons) which occur in thin films or nanostructures of noble metals such as silver [21, 25]. The introduction of metallic nanoparticles into OSCs has resulted in plasmonic resonant metallic nanostructures, and the surface plasmon resonance depends upon the shape, size, and distribution of the metal nanoparticles [25]. Additionally the plasmonic properties of the nanoparticles are characterized by an absorption band in the visible range of the electromagnetic spectrum [57].

There are two primary schemes for the excitation of surface plasmon polaritons (SPP), which is done to create coherent collective oscillation of conducting electrons surrounding the metallic surfaces [25].

In the first scheme, SPPs propagate along the metallic dielectric interface triggered by the incorporation of metallic nanostructures such as gratings or periodic arrays. In the second scheme surface plasmons are localized by noble metal nanoparticles (such as Ag), this results in localized surface plasmon resonance (LSPR) [21], which is the collective oscillation of the conduction electrons of the metallic particles. The resulting movement of conduction electrons upon excitation by incident light leads to the escalation of polarization charges on the particle surfaces, and acts as a restoring

force, allowing resonance to occur [25].

Hamdan *et al.* have observed that at wavelengths near the plasmon resonance peak, Ag-NPs strongly scatter light. Through this observation it can be seen that plasmon behaviour arises from the collective oscillation of free electrons in the metallic particle. At the surface plasmon resonance peak, the scattering cross section exceeds the geometrical cross section of the Ag particle, thus increasing the amount of light scattered into the cell. As a result, incident light of similar wavelength to that of the resonance wavelength of the particles is strongly absorbed [25].

The addition of NPs to the anodic buffer layer has previously shown an increase to the excitation of LSPR and enhancement of the overall PCE. It is also important to note that the addition of NPs has been shown to have negligible effect on the charge transport process [21].

In experiments conducted by Lee *et al.* strong evidence provided by steady state and photoluminescence (PL) measurements has shown that LSPR due to Au-NPs increases light absorption and enhances the degree of exciton dissociation. This therefore improves the photocurrent and overall device efficiency by exploiting the advantages gained through the optical effects of LSPR. As a result, the OSCs prepared by Lee *et al.* had the following advantages: enhanced broad light absorption, improved generation rate and dissociation efficiency, and increased charge carrier density and lifetime [21]. It should therefore be possible to generate similar such advantages and improved device performances using Ag-NPs.

Furthermore, it is important to note that few efficiencies above 8% have been observed through the incorporation of nanoparticles within OSCs [21].

2.5 Transition Metal Oxides as a Buffer Layer in Organic Solar Cells

Although using ITO as a transparent anode and PEDOT:PSS as a buffer layer has yielded results with enhanced device performances, there is one unfortunate flaw with this device setup. That is, the interface between ITO and PEDOT:PSS is unstable and as a result a chemical reaction occurs between the two materials. The reaction between the two materials can cause degraded device performance, and reduce the overall lifetime of the device [35, 58, 59, 60, 61].

Numerous TMOs have been used as a substitute for PEDOT:PSS, with MoO_3 , V_2O_5 , and WO_3 being the most widely used. The widespread use of the above three TMOs is due to their favorable electronic properties, low optical absorption in the visible spectrum and a high level of technological compatibility.

Additionally TMOs will often have good energy level alignment between themselves and the organic layers of the OSC. The result of this energy level alignment is improved hole-injection and extraction properties which helps to improve overall device performance [61].

While the vast majority of TMOs have seen significant research into their potential use in OSCs, CdO has stood out as having seen very minimal study. Despite this, CdO shows potential to be successfully used as an anodic buffer layer, due to its low band gap (2.31 eV at 298K [62]) and relatively high electron conductivity (~ 875 S/cm [63]). In fact CdO only has a slightly lower band gap than either MoO_3 , V_2O_5 , or WO_3 .

Chapter 3

Experimental Details

3.1 Introduction

In order to further expand the study of the effects of Ag-NPs on OSCs, cells consisting of 5, 10, 20, and 30 nm Ag-NPs were prepared. The Ag-NPs used were monodisperse, in aqueous solution with a concentration of 0.02 mg/mL, and were used as supplied by nanoComposix Inc. General cell preparation followed the above mentioned work of Hamdan *et al.*, however PCBM:P3HT was substituted as the active layer. Following this, Al was used as the cathode providing a reference sample with basic structure consisting of ITO/PEDOT:PSS/P3HT:PCBM/Al, as well as providing preliminary test samples with structure ITO/Ag-NP/PEDOT:PSS/P3HT:PCBM/Al. These results were then compared with the work previously completed by Hamden *et al.* [25], in order to ensure the success of the preliminary experimentation.

The next experiments were conducted in order to determine the effect that Ag-NPs would have on cell performance when doped into the P3HT:PCBM active layer. The result was solar cells with the structure ITO/PEDOT:PSS/P3HT:PCBM:Ag-NP/Al, where the Ag-NP sizes were varied in the same manner as the previous experiments.

Additionally tests were conducted using Ag-NPs as an interface layer between the PEDOT:PSS buffer layer and the P3HT:PCBM active layer, the result was a cell structure of ITO/PEDOT:PSS/Ag-NP/P3HT:PCBM/Al. Once again the Ag-NP sizes were varied in the same manner as the previous tests.

After the successful completion of these experiments, tests were conducted following from the work of Xie *et al.* [22] with the exception that Ag-NPs were substituted for Au-NPs. The result was that each of the Ag-NPs sizes was doped into the PEDOT:PSS layer, providing a structure of ITO/PEDOT:PSS:Ag-NP/P3HT:PCBM/Al which allowed the examination of their effects on the device performance.

The locations chosen for testing the effect of the Ag-NP sizes were selected due to the previous success of adding either Ag-NPs or gold nanoparticles in each of the respective layers [21, 22, 24, 25, 64, 65].

Upon the completion of the above experiments, subsequent experiments were completed in order to test the feasibility of using CdO as an anodic buffer layer. Therefore samples were prepared with the following structures, ITO/CdO/PCBM:P3HT/Al, ITO/TiO₂/PCBM:P3HT/CdO/Al, and ITO/TiO₂/PCBM:P3HT/MoO₃/Al. Furthermore the ITO/CdO/PCBM:P3HT/Al structure will be compared to the same reference sample that was used for the Ag-NP doping above. The ITO/TiO₂/PCBM:P3HT/MoO₃/Al structure was chosen because except for using Ag instead of Al, this structure has been successfully used as a reference device in the works of Siuzdak *et al.* and Li *et al.* [66, 67].

It is important to note that the second two structures are actually inverted solar cells and both contain TiO₂. These structures were selected in order to compare with and remain consistent with previous works studying TMOs as buffer layers for OSCs; MoO₃ was specifically chosen as part of the control samples because it has been previously used in numerous experiments such as those completed by Siuzdak

et al. [66], Shrotriya *et al.* [35], and Tan *et al.* [36].

Finally cells were to be fabricated using both TMOs and Ag-NPs, these cells were intended to determine the suitability of combining both methods of improving OSC performance. These combination cells would have had structures of ITO/CdO/P3HT:PCBM:Ag-NP/Al and ITO/TiO₂/P3HT:PCBM:Ag-NP/CdO/Al, in order to compare with both types of reference cell.

Furthermore, these cells would have been constructed using both 5 and 10 nm Ag-NPs, however due to the poor results obtained from the experiments testing the feasibility of using CdO as a buffer layer, tests on the combination cells were abandoned. This course of action was chosen due to the high likelihood that the combination cells would show no significant improvement over the poor results obtained from the CdO buffer layer cells.

3.2 Sample Preparation

In order to fabricate the required OSCs, it was first necessary to clean and pattern the ITO substrates (surface resistance $10 \pm 5 \Omega/sq$ purchased from Delta Technologies Limited). Cleaning the substrates was accomplished in the following manner, first the substrates were rinsed with distilled water, this was followed by a 10 minute sonication in baths of each of following: ethanol, acetone, and distilled water. The substrates were rinsed with distilled water after each bath. The substrates were then dried with compressed air before being baked at 200°C for a minimum of 2 hours.

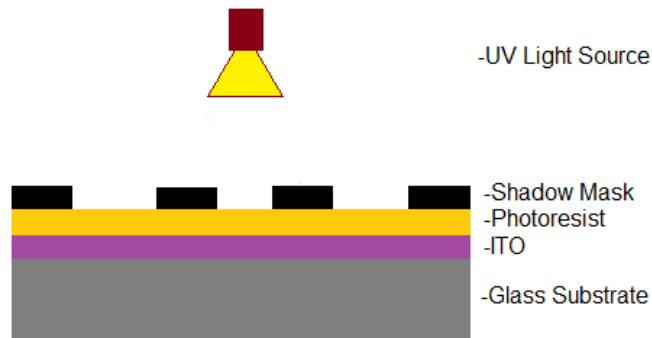
This cleaning process was chosen due to the ability of the selected solvents to remove any contaminants located on the substrates. The rinse with distilled water removed any lint of other larger contaminants, while the ethanol bath removed fingerprints, body oils or similar residual organic contaminants from the substrate.



(a) ITO substrate before photolithography.



(b) ITO substrate after spin coating Shipley 1813 positive photoresist.



(c) Shadow mask is placed on the substrate and UV light is applied.



(d) Substrate after sodium hydroxide bath.



(e) Substrate after etching with hydrochloric acid.



(f) ITO coated substrate with desired pattern after final cleaning.

Figure 3.1: Schematic diagram of photolithographic etching of ITO coated substrates.

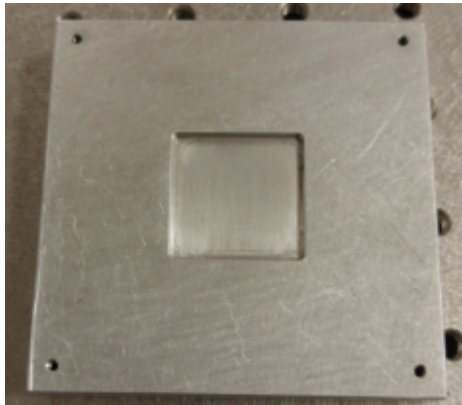
Acetone was then used to remove any remaining grease or other organic contaminants. The final sonication in distilled water removed any remaining contaminants as well as ensure all the ethanol and acetone was washed away. Drying with compressed air removed the bulk of the residual water before baking ensured the substrate was completely dry and contaminant free.

The patterning process was accomplished through photolithography using Shipley Microposit S1813 positive photoresist. This process is demonstrated in Figure 3.1 and was completed in the following manner. The S1813 photoresist was spin coated onto the substrate at 4000 rpm for 60 seconds, and was then soft baked at 100°C for 60 seconds. Soft baking is critical because it removes the solvents in the photoresist and the photoresist only becomes photosensitive after soft baking. The resulting structure from this process is demonstrated in Figure 3.1b.

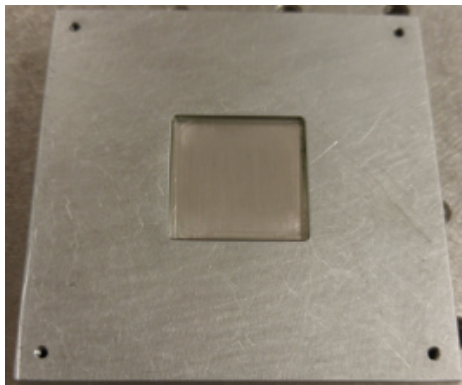
In order to ensure the correct etching pattern, the substrate was then placed into a custom substrate holder and shadow mask. The substrate holder and shadow mask were designed and fabricated specifically for this project and are demonstrated in Figure 3.2. The substrate was then exposed to UV-light from a mercury lamp for approximately 70 seconds, and the setup is shown in Figures 3.1c and 3.3.

The next step was developing the photoresist as well as removing any excess photoresist from the substrate. This was accomplished by removing the sample from the holder and placing it in a 0.5% Sodium Hydroxide (NaOH) bath until the S1813 that had been exposed to the UV-light turned a brown color, it was shaken slightly to remove the residue and the process was repeated until the color of the S1813 remained the same. The bathing process took between 10 and 20 seconds, and the process resulted in a structure similar to the one shown in the schematic demonstrated in Figure 3.1d.

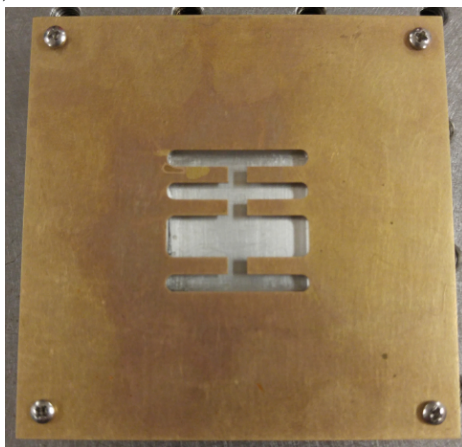
The substrate was then rinsed with distilled water to remove any residual sodium



(a) Empty substrate holder.



(b) Substrate holder with ITO substrate.



(c) Substrate holder and attached shadow mask.

Figure 3.2: Homemade substrate holder and shadow mask.

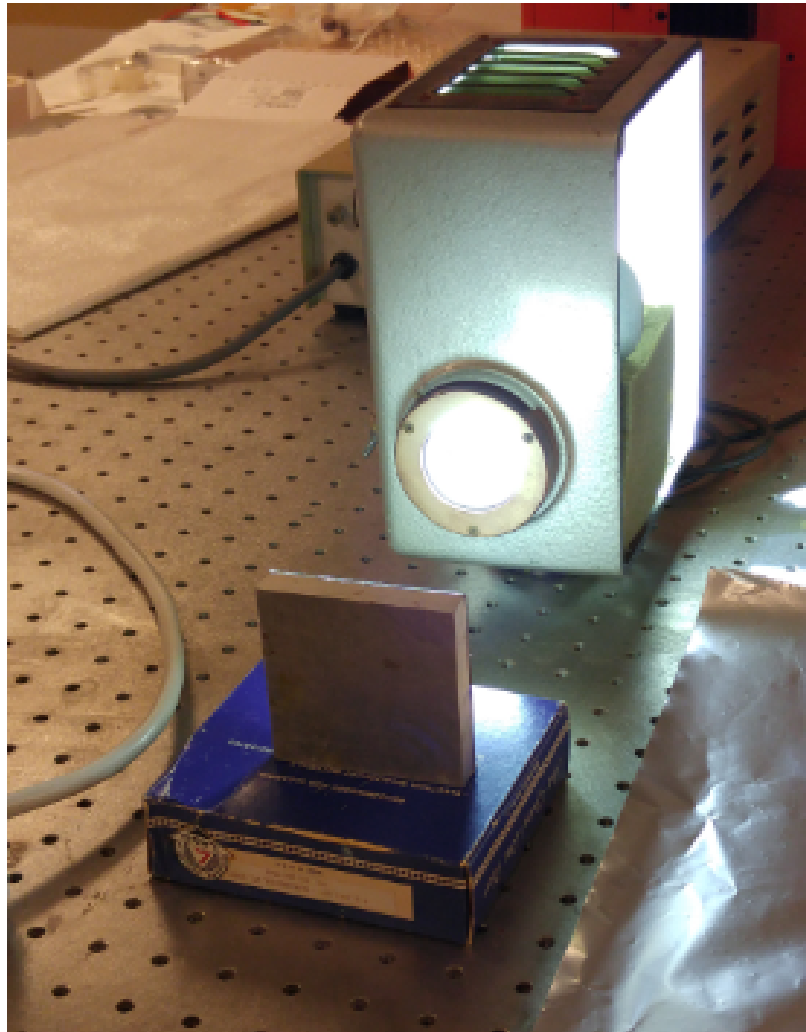


Figure 3.3: Mercury lamp and substrate (in holder with shadow mask) during UV exposure portion of the photolithographic process.

hydroxide before being bathed in hydrochloric acid for ~ 3 minutes to remove the ITO which was left exposed after the sodium hydroxide bath. The substrate was rinsed with distilled water to remove the residual hydrochloric acid and was then inspected visually and with a multimeter to ensure the correct pattern had been obtained. A schematic of the resulting structure is demonstrated in Figure 3.1e.

Finally the substrate was cleaned in the same manner as previously mentioned, removing the remaining S1813 and leaving the desired pattern on the ITO substrate.

A schematic representation of the resulting structure from this step is demonstrated in Figure 3.1f.

3.2.1 Control Samples

Control samples with a structure of ITO/PEDOT:PSS/P3HT:PCBM/Al were prepared through the following process. The PEDOT:PSS (Clevios PV P AI4083) solution was filtered through a $0.45\ \mu\text{m}$ filter, the filtered solution was then deposited onto the ITO substrate by spin coating at 3500 rpm for 120 s. The substrate was subsequently annealed on a hot plate at 150°C for 10 min.

The active layer solution was prepared beforehand by mixing P3HT and PCBM with a 1:1 weight ratio and using 1,2-dichlorobenzene (ODCB) as a solvent. The P3HT was supplied by Rieke Metals Inc. (catalog number 4002-E) and the PCBM was C_{60}PCBM (PC_{60}BM) supplied by Nano-C. The P3HT:PCBM solution was stirred overnight before being filtered through a $0.45\ \mu\text{m}$ filter.

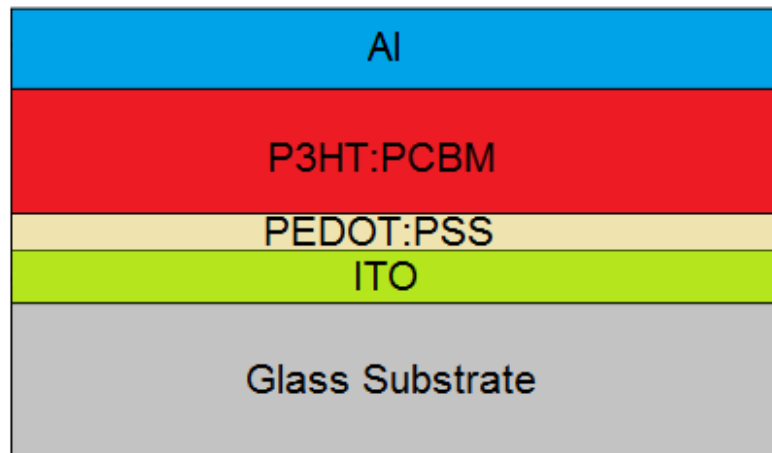
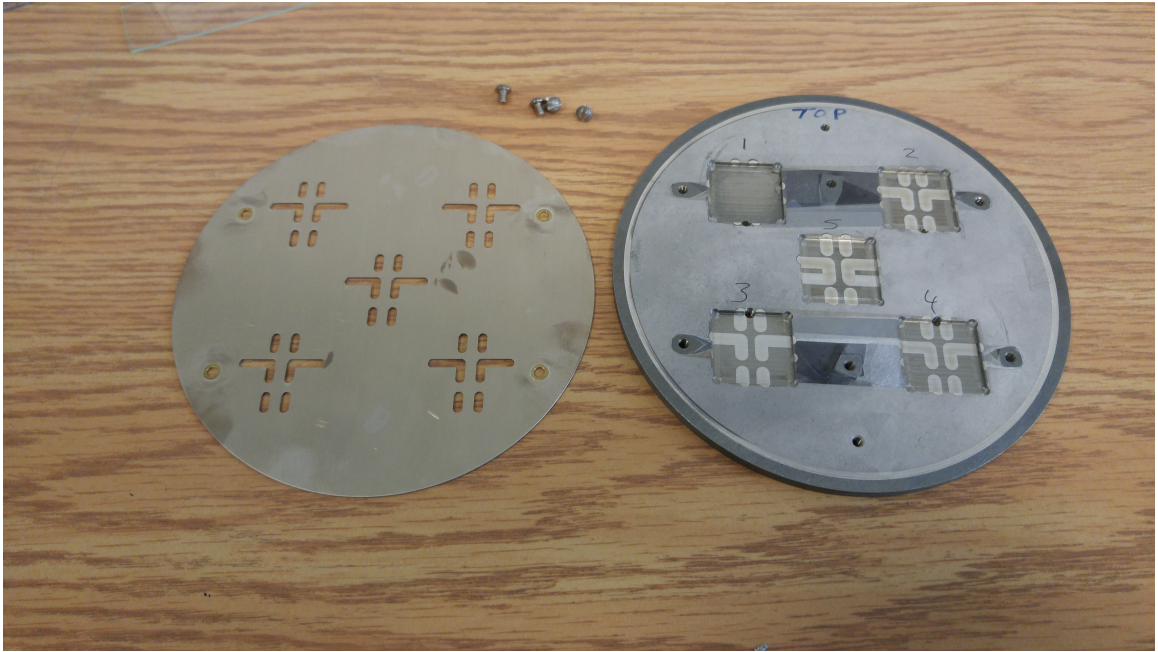


Figure 3.4: Structure diagram of control cells.

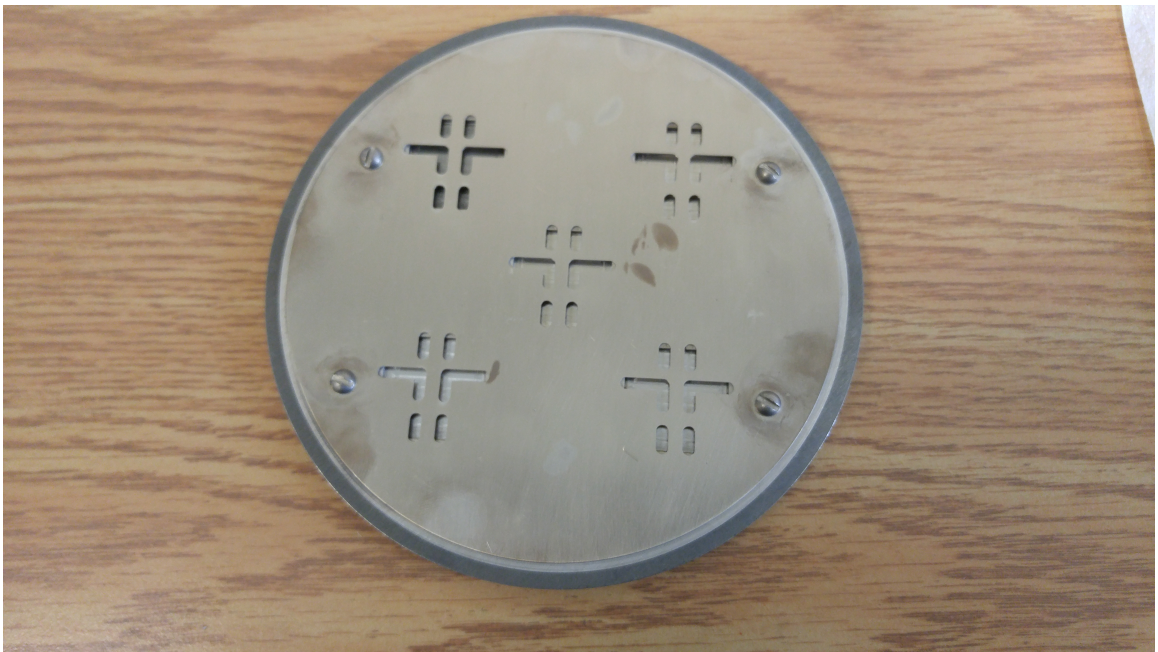
After the substrate had cooled the filtered P3HT:PCBM solution was applied through spin coating at 800 rpm for 40 s, followed by annealing at 150°C for 10 min.

Additionally the 100 nm thick Al cathode was applied using thermal evaporation in a vacuum chamber at approximately 10^{-8} Torr. In order to achieve the desired Al pattern the thermal evaporation took place through a shadow mask that was designed and fabricated as part of this project, and it is demonstrated in Figure 3.5. Finally the cell was annealed at 150°C for 10 min before being allowed to cool to room temperature in a covered petri dish [24, 25, 68]. The final structure for the control devices is demonstrated in Figure 3.4.

During each stage of the fabrication process a test sample was prepared and used to measure the thickness of each layer. These measurements were taken using Zygo Nexview Optical Surface Profiler. Furthermore the combination of the shadow masks used for the photolithography (Figure 3.2) and for the deposition of Al (Figure 3.5) gave a final cell size of 9 mm^2 .



(a) Homemade substrate holder and shadow mask.



(b) Substrate holder and attached shadow mask ready to be placed in vacuum chamber.

Figure 3.5: Shadow mask used for the thermal evaporation of the Al cathode.

3.2.2 Silver Nanoparticle Cells

Following the same cell structure as Hamdan *et al.*, the preliminary test cells were prepared in the following manner [25]; Ag-NPs were deposited onto the patterned ITO using spin coating at 2500 rpm for 60 s. It is important to note that multiple cells were created simultaneously with each of the different sized Ag-NPs, thus allowing experiments to be conducted independently on each of the 5, 10, 20, and 30 nm Ag-NPs. Following the spin coating of the Ag-NPs, the substrates were annealed at 150°C for 10 min.

After annealing, the substrate was allowed to cool back down to room temperature, once this was completed the PEDOT:PSS, P3HT:PCBM, and Al layers were applied following the same procedure as given in Section 3.2.1 for the control devices. The resulting cell structure is presented in Figure 3.6.

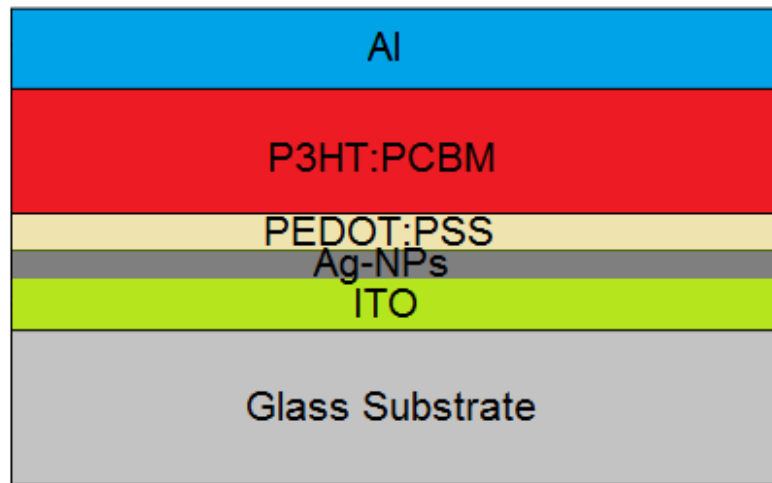


Figure 3.6: Structure diagram of ITO/Ag-NP/PEDOT:PSS/P3HT:PCBM/Al cells.

After testing had been completed on the above cells, additional cells were created by incorporating the Ag-NPs into the P3HT:PCBM active layer. The P3HT:PCBM:Ag-NP solution was prepared by combining P3HT:PCBM solution and each of the

aqueous Ag-NP solutions in a 2:1 volume ratio prior to mixing overnight.

After mixing, the solution was allowed to sit for ~ 1 hour, after which the remaining water (since it is immiscible with the P3HT:PCBM solution) was carefully siphoned off. What remained was a solution of P3HT:PCBM and Ag-NPs. This solution was then spin coated at 800 rpm for 40 s onto previously prepared PEDOT:PSS coated substrates. The substrate was then annealed for 10 min at 150°C , after which the Al cathode was applied. The PEDOT:PSS and Al layers were applied using the same methods as given in Section 3.2.1, and the final device structure as demonstrated in Figure 3.7 was ITO/PEDOT:PSS/P3HT:PCBM:Ag-NP/Al.

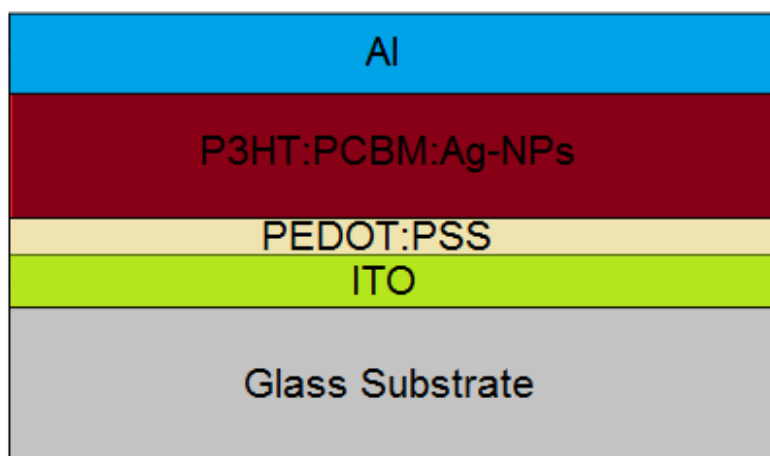


Figure 3.7: Structure diagram of ITO/PEDOT:PSS/P3HT:PCBM:Ag-NP/Al cells.

The next structure tested placed a separate layer of Ag-NPs between the PEDOT:PSS and P3HT:PCBM layers and resulted in a cell structure of ITO/PEDOT:PSS/Ag-NP/P3HT:PCBM/Al, which is demonstrated in Figure 3.8. For this structure the Ag-NPs were spin coated at 2500 rpm for 60 s onto the previously prepared PEDOT:PSS coated substrate. Once the Ag-NPs were applied the substrate was once again annealed at 150°C for 10 min before the P3HT:PCBM and Al layers were applied. Much like for the previously prepared devices, the application of the PE-

DOT:PSS, P3HT:PCBM, and Al layers followed the same procedure given in Section 3.2.1.

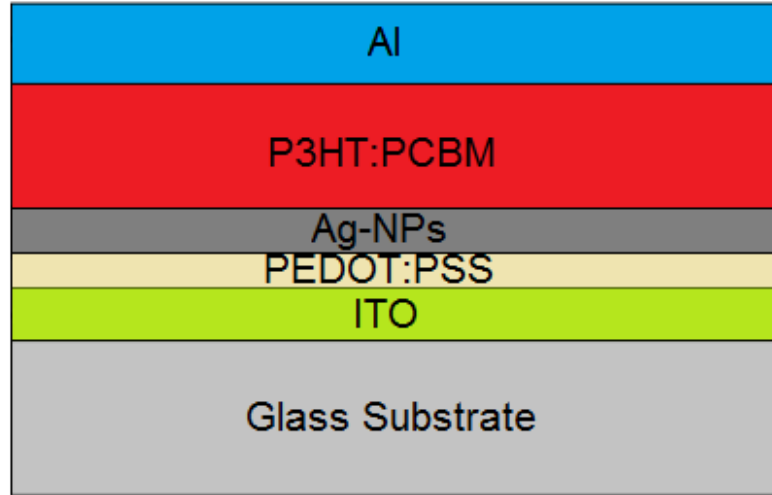


Figure 3.8: Structure diagram of ITO/PEDOT:PSS/Ag-NP/P3HT:PCBM/Al cells.

The final structure consisting of Ag-NPs that was tested had the Ag-NPs doped into the PEDOT:PSS layer. The doping was accomplished by combining the PEDOT:PSS and aqueous Ag-NP solutions in a 2:1 volume ratio and then stirring the solution for two hours.

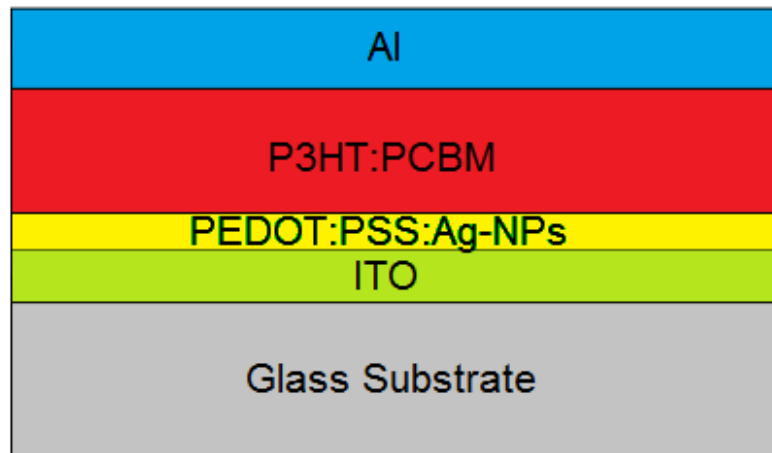


Figure 3.9: Structure diagram of ITO/PEDOT:PSS:Ag-NP/P3HT:PCBM/Al cells.

Once the mixing was complete the PEDOT:PSS:Ag-NP solution was spin coated at 3500 rpm for 120 s onto the prepared ITO substrate. After spin coating, the substrate was annealed at 150°C for 10 min and then allowed to cool to room temperature. The P3HT:PCBM and Al layers were once again applied using the same procedures as given in Section 3.2.1, which resulted in the final structure given in Figure 3.9.

3.2.3 Transition Metal Oxide Cells

Once the testing on the cells containing Ag-NPs was complete, the cells containing the TMOs and specifically CdO were prepared. The CdO was prepared as a suspension (5 mg/mL) in dimethyl sulphoxide (DMSO). The CdO solution was then spin coated at 1500, 2500, and 3500 rpm onto separate pre-prepared ITO substrates. Subsequently the substrates were annealed at 150 °C for 10 min.

The P3HT:PCBM active layer, as well as the Al cathode layer were then prepared and applied using the same procedure as given previously in Section 3.2.1. The result of this process was the desired structure of ITO/CdO/P3HT:PCBM/Al which is demonstrated in Figure 3.10.

After testing the above cells, two additional sets of cells were then fabricated. The first set of cells was prepared in the following manner: TiO₂ was spin coated from a dispersion (5mg/ml) in DMSO onto the prepared ITO substrate at 5000 rpm for 60s [66], this was followed by thermal annealing on a hot plate at 150°C for 10 min to remove any residual solvent.

The P3HT:PCBM and CdO layers were then applied using the same procedures as given previously, with the exception being that the CdO was applied after the P3HT:PCBM. An Al electrode was then applied through thermal evaporation using

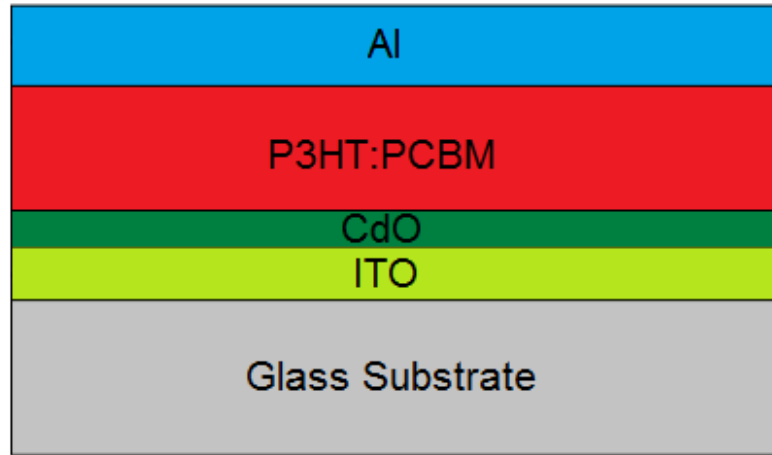


Figure 3.10: Structure diagram of ITO/CdO/P3HT:PCBM/Al cells.

the same shadow mask as shown in Figure 3.5. The result was the inverted cell structure of ITO/TiO₂/P3HT:PCBM/CdO/Al which is shown in Figure 3.11.

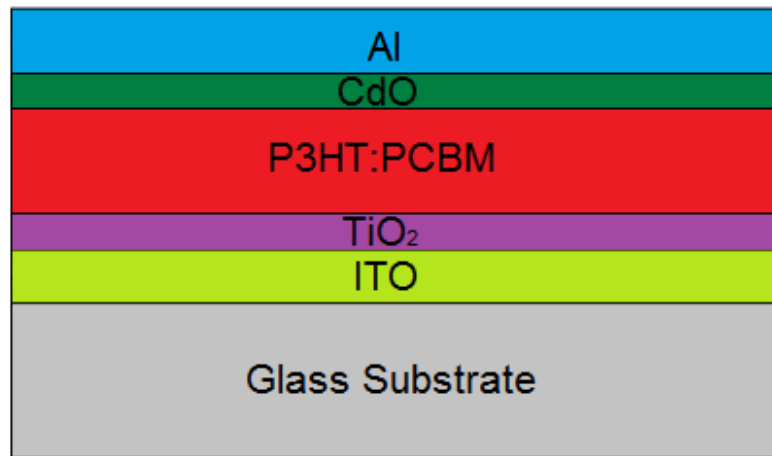


Figure 3.11: Structure diagram of ITO/TiO₂/P3HT:PCBM/CdO/Al cells.

The reference inverted solar cell was then fabricated using the following procedure: the TiO₂ and P3HT:PCBM were applied using the same procedure as the previous samples. Subsequently the MoO₃ which had been previously prepared as a 5 mg/ml suspension in isopropanol, was then spin coated on top of the active layer at 4000 rpm for 60 s [36], the substrate was then annealed at 150°C for 10 minutes.

The Al electrode was once again applied via thermal evaporation through the previously shown shadow mask (Figure 3.5), the result being the structure demonstrated in Figure 3.12, which is ITO/TiO₂/PCBM:P3HT/MoO₃/Al as desired.

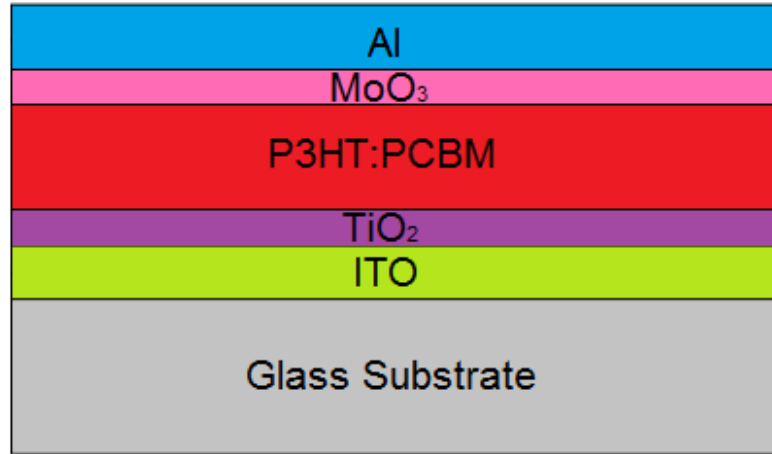


Figure 3.12: Structure diagram of ITO/TiO₂/PCBM:P3HT/MoO₃/Al cells.

3.2.4 Nanoparticle and Transition Metal Oxide Cells

The final experiments that were to be conducted during this project were intended to combine the use of both Ag-NPs and TMOs in an effort to produce an even more efficient OSC. Each layer of these combination cells was to be prepared using the same procedure that was given for the previous tests. The resulting structures were to be ITO/CdO/P3HT:PCBM:Ag-NP/Al and ITO/TiO₂/P3HT:PCBM:Ag-NP/CdO/Al respectively.

However upon completion of the tests on the ITO/CdO/P3HT:PCBM/Al, ITO/TiO₂/P3HT:PCBM/CdO/Al, and ITO/TiO₂/P3HT:PCBM/MoO₃/Al cells, the tests combining the Ag-NPs and CdO were abandoned due to the extremely poor performances achieved these experiments. Further details on these experiments is presented in Chapter 4.

3.3 Testing

Once the OSCs were prepared their current density-voltage (J-V) curves were measured with a Keithley 2420 SourceMeter under simulated AM 1.5G irradiation (100 mW/cm^2) from a xenon-lamp-based solar simulator (Newport Oriel 96000 250W solar simulator) with filters. Current density-voltage curves provide information on the relationship between the current through, and the voltage across the solar cell.

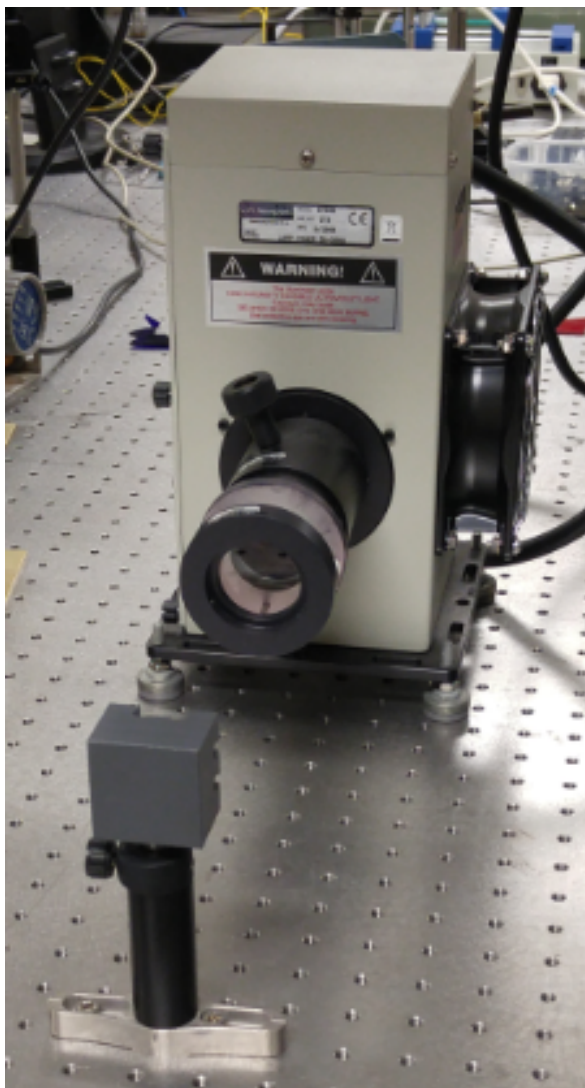


Figure 3.13: AM 1.5G solar simulator used during the testing of cell efficiency.

Examining this information allows for greater understanding of the basic parameters of the cells, and provides the information required for the performance of the cells to be determined. The simulated AM 1.5G light is designed to simulate the average spectral irradiance on the earth at mid-latitudes and has been one of two standardized terrestrial spectra since the 1970s [69].



Figure 3.14: Computer and Keithley 2420 source meter (under the keyboard) used for testing cell efficiency.

The Keithley 2420 was controlled with a computer using LabView, and the entire setup is demonstrated in Figures 3.13 and 3.14. The J-V curves acquired from

LabView were then examined using Mathematica 10.3 [70] in order to accurately determine the short circuit current density (J_{SC}), open circuit voltage (V_{OC}), fill factor (FF), and the power conversion efficiency (PCE).

Chapter 4

Results and Discussion

In order to determine the effectiveness of each of the methods tested in this work it was necessary to accurately calculate the power conversion efficiency (PCE) of each device. This calculation is completed by examining the produced current density-voltage (J-V) curve and obtaining the open circuit voltage (V_{OC}), short circuit current density (J_{SC}), and the maximum power point (P_{Max}).

The maximum power point is the maximum obtainable power from the solar cell and is represented by the area encompassed within the red rectangle in Figure 4.1. The maximum power point is calculated using the V_{Max} and J_{Max} which are located at points B and C respectively in Figure 4.1; mathematically the P_{Max} is the maximum rectangular area under the given J-V curve.

Using this information it is then possible to calculate the fill factor (FF) for the given cell. The FF is essentially the measure of the quality of a cell and is one of the key parameters for determining the efficiency of a solar cell. Fill factor is defined as the ratio between the P_{Max} and the theoretical maximum power, with the theoretical maximum power being the product of the V_{OC} and the J_{SC} which are located at points A and D respectively in Figure 4.1 [71]. The equation required for calculating

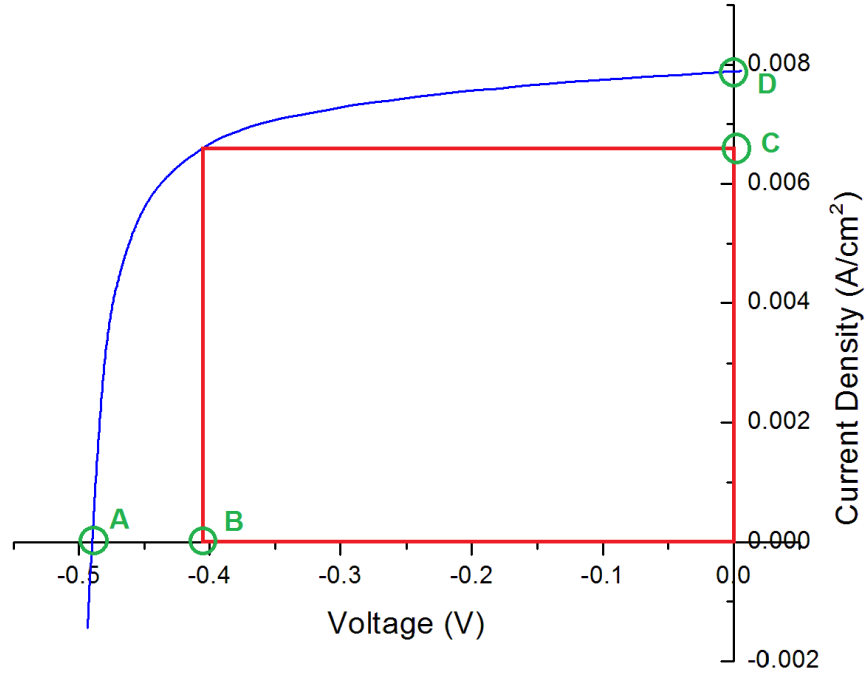


Figure 4.1: J-V curve demonstrating the calculation of V_{OC} (A), V_{Max} (B), J_{Max} (C), and J_{SC} (D).

FF is presented in Equation (4.1).

$$FF = \frac{J_{Max} V_{Max}}{J_{SC} V_{OC}} \quad (4.1)$$

It is then possible to calculate the PCE, which is the percentage of solar energy that is converted to electricity by a particular solar cell. This calculation is completed using Equations (4.2) and (4.3), where η is the PCE of the cell and P_{In} is 100 mW/cm^2 which is the input power from the solar simulator.

$$\eta = \frac{P_{Max}}{P_{In}} * FF * 100\% \quad (4.2)$$

$$\frac{P_{Max}}{P_{In}} = \frac{J_{SC} V_{OC}}{100 \frac{mW}{cm^2}} \quad (4.3)$$

4.1 Control Cells

Control samples with a structure of ITO/PEDOT:PSS/P3HT:PCBM/Al were examined in order to compare with subsequent experiments. First, however, preliminary experiments were conducted to determine the best spin coat speeds and thus thickness for the respective PEDOT:PSS and P3HT:PCBM layers. This was done in order to ensure the highest possible starting PCE for the OSCs.

Cells were prepared with a set P3HT:PCBM spin coat speed of 700 rpm, and the PCE was examined for PEDOT:PSS layers spin coated at 1000, 1500, 2000, 2500, 3000, 3500, and 4000 rpm. The best results were achieved at a speed of 3500 rpm which gave a thickness of 40 ± 5 nm. Using this 3500 rpm spin coat speed for the PEDOT:PSS, spin coating speeds of 500, 600, 700, 800, 900, and 1000 were then tested for the P3HT:PCBM active layer, and the PCE examined once again. The result was that spin coating the P3HT:PCBM at 800 rpm gave the highest PCE, as well as a thickness of 190 ± 10 nm.

The combination of spin coating the PEDOT:PSS and P3HT:PCBM at 3500 and 800 rpm respectively was selected for the control samples, and the result was an average PCE of 2.40% and an average FF of 0.574. A J-V curve taken from one of the control samples is demonstrated in Figure 4.2.

Furthermore, the control cells gave an average J_{SC} of 7.2 mA/cm² and an average

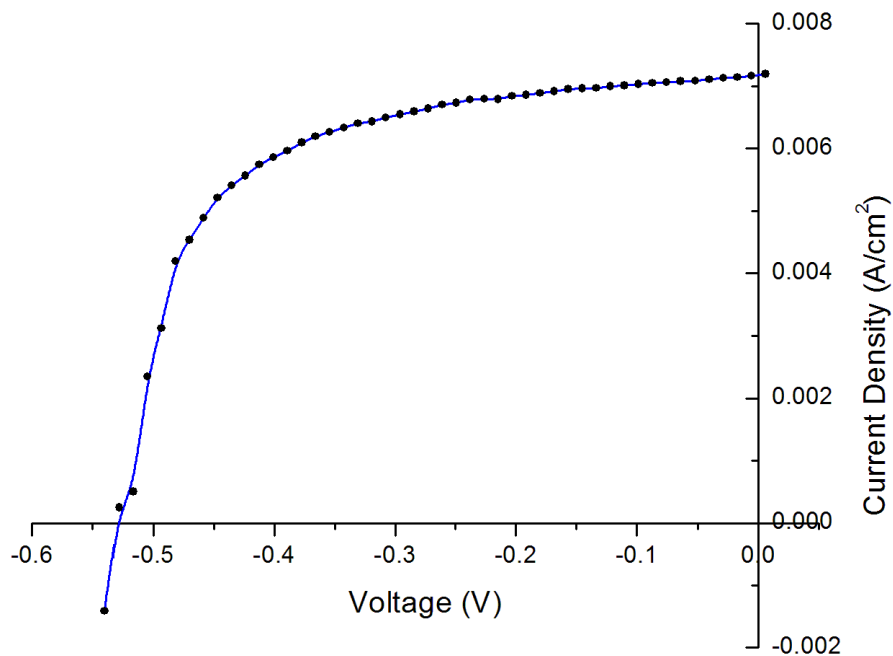


Figure 4.2: J-V curve for control samples, with structure of ITO/PEDOT:PSS/P3HT:PCBM/Al.

V_{OC} of 0.60 V, as well as an average J_{Max} of 7.2 mA/cm² and average V_{Max} of 0.46 V.

The experimental uncertainties for the control cells were $\pm 0.04\%$ for the PCE, ± 0.005 for the FF, ± 0.1 mA/cm² for the J_{SC} and J_{Max} , and ± 0.01 V for the V_{OC} and V_{Max} . Additionally, the experimental uncertainties for each of the subsequent experiments were the same as those of the control devices.

4.2 Incorporation of Silver Nanoparticles into Organic Solar Cells

The first cells consisting of Ag-NPs to be tested had the NPs applied directly onto the ITO prior to the application of the PEDOT:PSS, P3HT:PCBM, and Al layers. The next set of tests consisted of doping the Ag-NPs into the P3HT:PCBM active layer; followed by tests where a layer of Ag-NPs was applied onto the PEDOT:PSS before adding the active layer. Finally, cells were prepared by doping the Ag-NPs into the PEDOT:PSS prior to applying the Ag-NP doped PEDOT:PSS, P3HT:PCBM, and Al layers.

It is important to note that a minimum of three substrates consisting of six individual cells (18 total cells) were tested for the desired structures.

4.2.1 ITO/Ag-NP/PEDOT:PSS/P3HT:PCBM/Al Cells

Following fabrication, the devices constructed using 5 nm Ag-NPs were exposed to the solar simulator and their respective J-V curves were examined. A J-V curve for the tested cells is shown in Figure 4.3.

The result of these tests produced an average PCE of 2.60%, with a maximum efficiency of 2.70% being achieved twice. Additionally these devices provided an average FF of 0.586, an average J_{SC} and V_{OC} of 6.5 mA/cm² and 0.67 V, and an average J_{Max} and V_{Max} of 6.5 mA/cm² and 0.53V respectively. These results represent an 8.3% improvement in the average efficiency and a 12.5% improvement in the maximum PCE as compared to the control samples.

Furthermore there is a 2.0% improvement in FF and a 12% increase in the average V_{OC} for the cells with the NPs, unfortunately however there is a 9.7% decrease in the

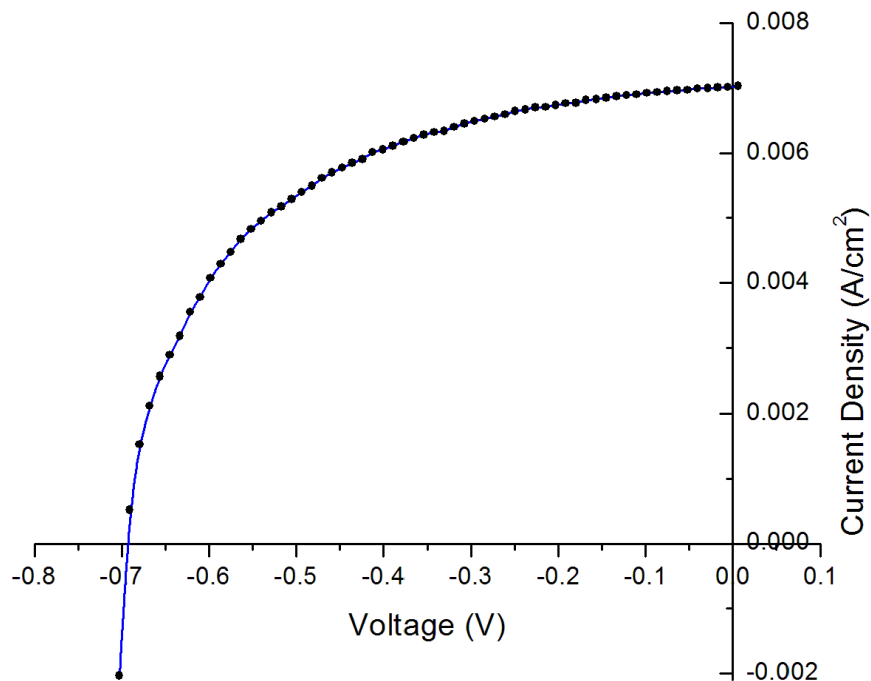


Figure 4.3: J-V curve for 5 nm samples, with structure of ITO/Ag-NP/PEDOT:PSS/P3HT:PCBM/Al.

average J_{SC} of the NP devices. Additionally, the J_{Max} and V_{Max} show a decrease of 9.6% and an increase of 21% respectively.

For devices constructed using the 10 nm Ag-NPs, the resulting average PCE was 2.57% and the maximum achieved PCE was 2.89%. These results were accompanied by an average FF of 0.586, and Figure 4.4 gives a J-V curve taken from these experiments.

These cells also delivered an average J_{SC} of 7.2 mA/cm², an average V_{OC} of 0.61 V, an average J_{Max} of 7.2 mA/cm², and average V_{Max} of 0.49 V. Comparing the results with the control samples showed a 7.1% improvement in average PCE, and

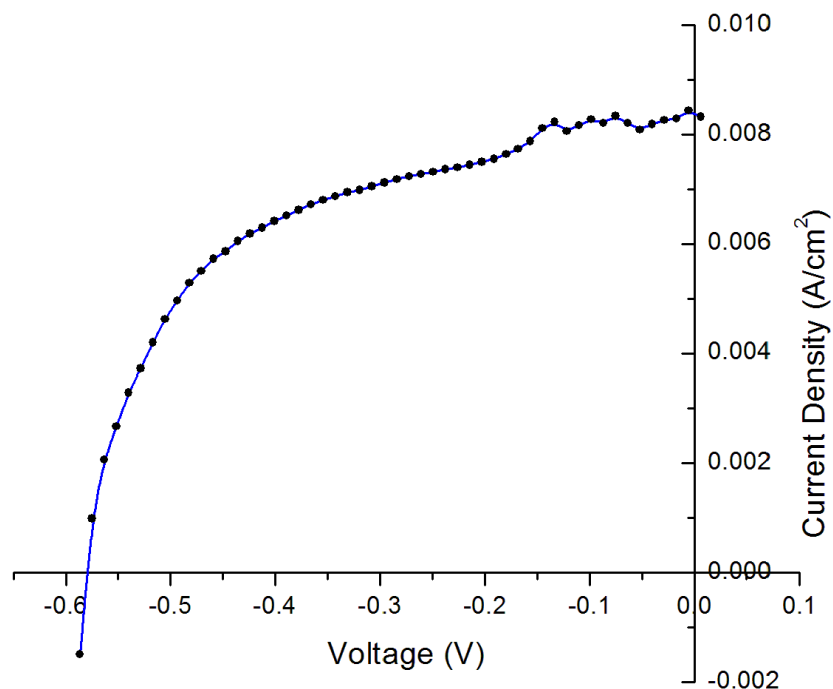


Figure 4.4: J-V curve for 10 nm samples, with structure of ITO/Ag-NP/PEDOT:PSS/P3HT:PCBM/Al.

a 20% improvement of the maximum PCE as compared to the average PCE of the control devices. Additionally these devices produced an increase of 1.7% and 5.6% in V_{OC} and V_{Max} respectively, as well as a 2.0% increase in FF. However the average J_{SC} and J_{Max} was the same as for the control devices.

The average and maximum PCE of the devices constructed using the 20 nm Ag-NPs was 2.49% and 2.88% respectively, which corresponds to improvements of 3.8% and 20%. These devices also produced an average FF of 0.629 which was an increase of 9.5% over the control cells, and an example of a J-V curve for these devices is shown in Figure 4.5.

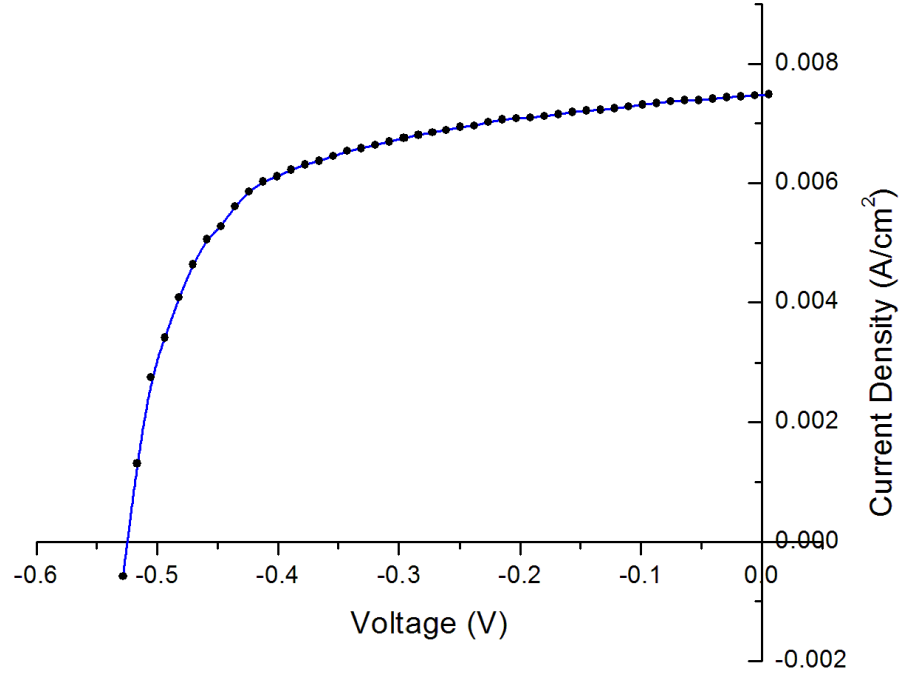


Figure 4.5: J-V curve for 20 nm samples, with structure of ITO/Ag-NP/PEDOT:PSS/P3HT:PCBM/Al.

The resulting average J_{SC} and V_{OC} were 7.1 mA/cm² and 0.57 V which corresponded with a decrease of 1.4% and an increase of 1.7% respectively. While the average J_{Max} and V_{Max} were 7.1 mA/cm² and 0.46 V, which was a decrease of approximately 1% for the J_{Max} , while the V_{Max} remained the same as the control samples.

Finally, cells were constructed using 30 nm Ag-NPs and these resulted in an average PCE of 2.52% and maximum PCE of 2.81%. These cells also provided a FF of 0.668, and a J-V curve for them is shown in Figure 4.6.

Additionally, the tests on these cells resulted in an average J_{SC} and V_{OC} of 7.1 mA/cm² and 0.55 V, while the J_{Max} and V_{Max} were 7.1 mA/cm² and 0.45 V. Overall

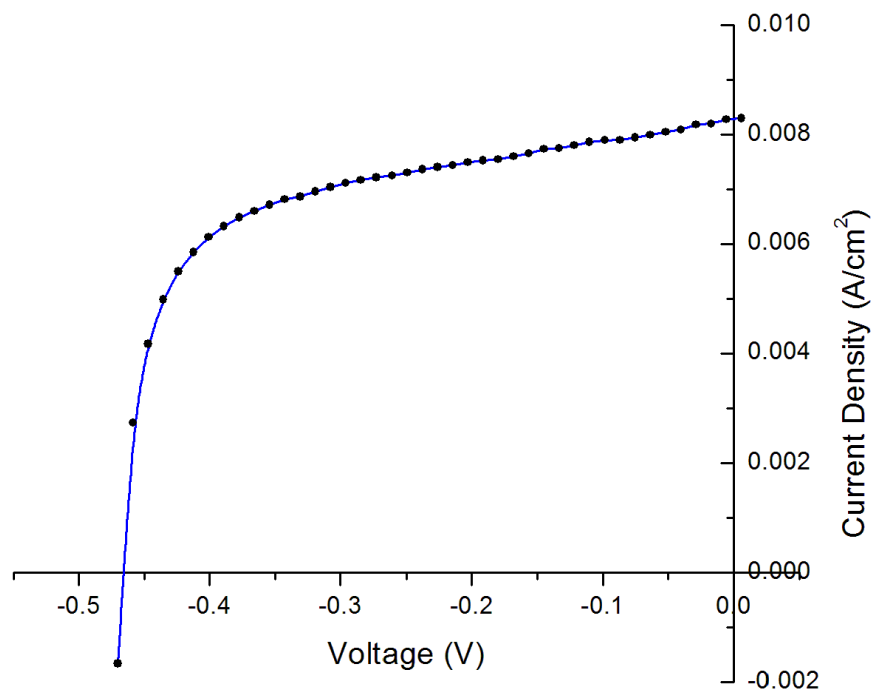


Figure 4.6: J-V curve for 30 nm samples, with structure of ITO/Ag-NP/PEDOT:PSS/P3HT:PCBM/Al.

these results were an increase in average and maximum PCE of 5.0% and 17%, an increase of 16% in FF, and a decrease of 1% in J_{SC} as compared to the control samples. Additionally there was a decrease of 5% in the V_{OC} , 1% in J_{Max} , and 2% in V_{Max} for these devices.

As can be seen in Table 4.1, there are several distinct patterns demonstrated in the results for the substrates coated with Ag-NPs. Specifically, each of the devices had an improved average PCE as compared to the control devices with a minimum improvement of 3.8% and a maximum of 8.3%. Additionally, the maximum PCE of the devices ranged from 12.5 - 20% higher than that of the control samples.

	PCE (%)	PCE _{Max} (%)	FF	J _{SC} (mA/cm ²)	V _{OC} (V)	J _{Max} (mA/cm ²)	V _{Max} (V)
Control	2.40		0.574	7.2	0.60	7.2	0.46
5 nm Ag-NP Cells	2.60	2.70	0.586	6.5	0.67	6.5	0.53
10 nm Ag-NP Cells	2.57	2.89	0.586	7.2	0.61	7.2	0.49
20 nm Ag-NP Cells	2.49	2.88	0.629	7.1	0.57	7.1	0.46
30 nm Ag-NP Cells	2.52	2.81	0.668	7.1	0.57	7.1	0.45

Table 4.1: Table of results for ITO/Ag-NP/PEDOT:PSS/P3HT:PCBM/Al cells.

This improvement in the efficiency of these devices is most likely a result of the plasmonic properties of the Ag-NPs enhancing light scattering within the cells. This enhanced scattering provides an improvement to the light trapping within the devices, and allows for the absorption of increased amounts of light. The increased absorption promotes the conversion of increased amounts of light energy into electricity. These results are consistent with previous work completed by Hamdan *et al.* [25].

Additionally, an in depth study into the effects of the plasmonic properties of nanoparticles and how they contribute to the efficiency of OSCs has been previously completed by Yoon *et al.* [72] and Kumar *et al.* [73].

Furthermore, the improvements to the FF of the devices is likely the result of a decrease in the series resistance within the devices resulting from the incorporation of the Ag-NPs. Equation (4.2) shows that there is a direct relation between the FF and the PCE of the devices, therefore the improvements to each device's PCE is likely a direct result of the FF improvement.

Additionally, since the fluctuations in J_{SC} , V_{OC} , J_{Max} , and V_{Max} are small for each of the devices, it is quite likely that they are simply a result of normal fluctuations within the devices. As a result it is believed that the presence of the Ag-NPs makes no significant contribution to the changes in these parameters.

4.2.2 ITO/PEDOT:PSS/P3HT:PCBM:Ag-NP/Al Cells

There was an improvement in the PCE for the devices constructed using an active layer of P3HT:PCBM doped with 5 nm Ag-NPs, prepared in a 2:1 volume ratio as discussed in Section 3.2.2. These devices resulted in an average PCE of 2.53% and a maximum PCE of 2.90%, which corresponded to an increase of 5.4% and 21% respectively. The resulting average FF for these devices was 0.507, which was

a 12% decrease as compared to the control cells. A J-V curve for these devices is demonstrated in Figure 4.7.

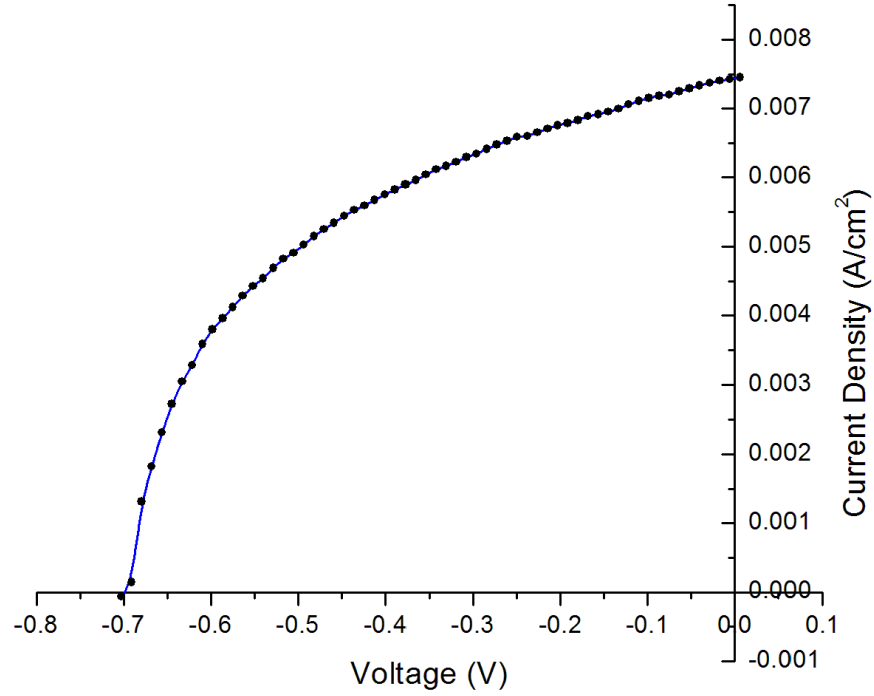


Figure 4.7: J-V curve for 5 nm samples, with structure of ITO/PEDOT:PSS/P3HT:PCBM:Ag-NP/Al.

There was also a J_{SC} of 7.7 mA/cm², a V_{OC} of 0.65 V, a J_{Max} of 7.7 mA/cm² and a V_{Max} of 0.47 V. These results corresponded to improvements of 6.9%, 8.3%, 6.9%, and 2.2% respectively for the J_{SC} , V_{OC} , J_{Max} , and V_{Max} .

The results for the devices with an active layer doped by 10 nm Ag-NPs provided an increase in the average PCE, maximum PCE, and FF for the devices. The average PCE for the devices was 2.64%, the maximum PCE was 2.88%, and the average FF was 0.608. These results corresponded with a improvements of 10%, 20%, and 5.9%

respectively. The J-V curve shown in Figure 4.8 is representative of these results.

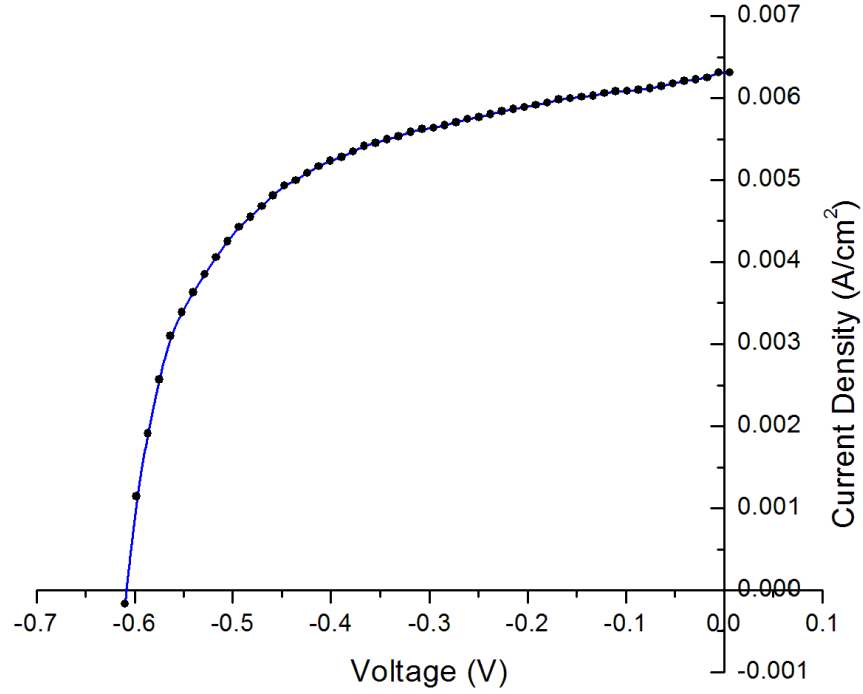


Figure 4.8: J-V curve for 10 nm samples, with structure of ITO/PEDOT:PSS/P3HT:PCBM:Ag-NP/Al.

Additionally, these cells had an average J_{SC} of 7.1 mA/cm² and V_{OC} of 0.61 V, corresponding to a decrease of 1% and an increase of 2% respectively. Furthermore there was an average J_{Max} of 7.1 mA/cm² and V_{Max} of 0.48 V; a decrease of 1% and improvement of 4.3% respectively over the control devices.

Using 20 nm Ag-NPs to dope into the active layer of the cells provided small improvements of 2.1% in average PCE and 3.3% to the FF of the devices. The corresponding average PCE and FF were 2.45% and 0.593, with the max PCE being 2.85%; an improvement of 19%. The J-V curve shown in Figure 4.9 is representative

of the results obtained for these devices.

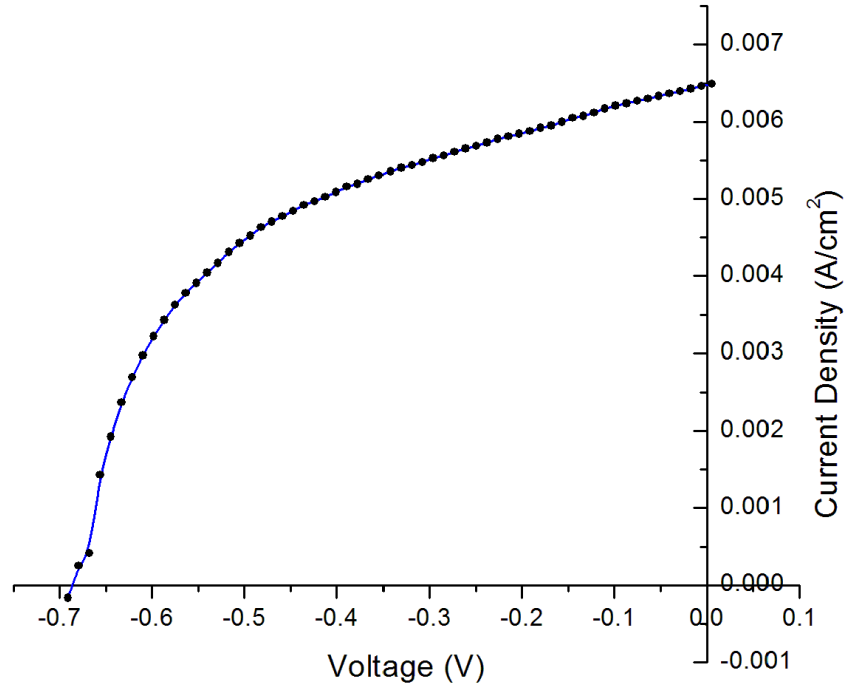


Figure 4.9: J-V curve for 20 nm samples, with structure of ITO/PEDOT:PSS/P3HT:PCBM:Ag-NP/Al.

The 20 nm Ag-NP doped cells also provided an average J_{SC} of 6.5 mA/cm², a V_{OC} of 0.60 V, a J_{Max} of 6.5 mA/cm², and a V_{Max} of 0.50 V. These results corresponded to a decrease in J_{SC} and J_{Max} of 9.7%, an improvement in V_{Max} of 8.7%, while the V_{OC} remained the same as in the control devices.

The final cells tested during this portion of the experimentation were constructed using 30 nm Ag-NPs. These cells produced an average PCE of 2.64% and a maximum PCE of 2.75%, additionally these cells provided a FF of 0.612. These results represent an improvement of 10%, 15%, and 6.6% respectively, and a J-V curve for these devices

is presented in Figure 4.10.

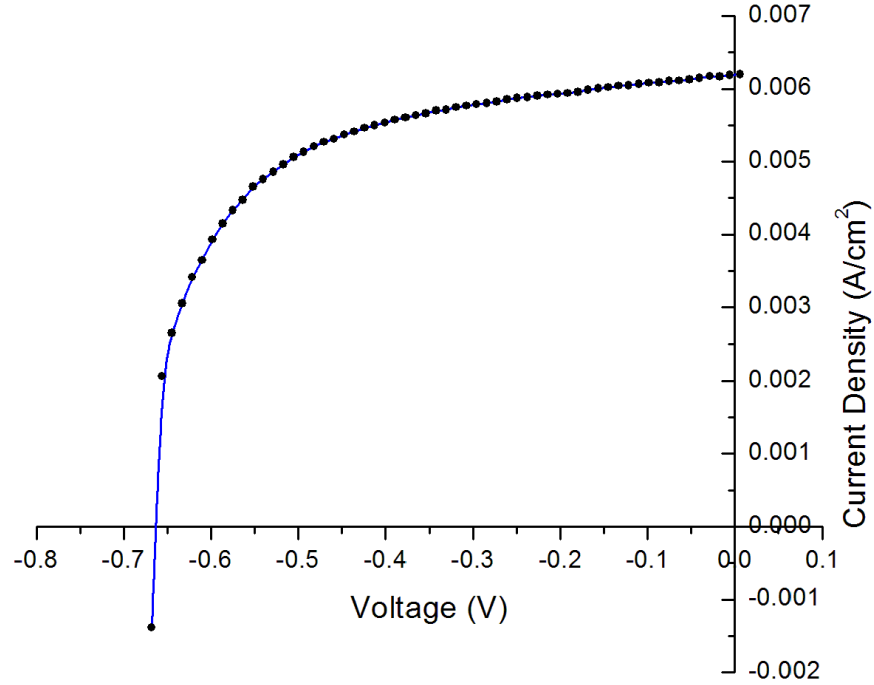


Figure 4.10: J-V curve for 30 nm samples, with structure of ITO/PEDOT:PSS/P3HT:PCBM:Ag-NP/Al.

Additionally, these devices resulted in a J_{SC} of 6.7 mA/cm² and a V_{OC} of 0.65 V which corresponded to a decrease of 6.9% and an increase of 8.3% respectively. Furthermore the J_{Max} and V_{Max} were 6.7 mA/cm² and 0.53 V which was a 6.9% decrease and 15% increase respectively.

There was an overall improvement to the performance of the OSCs by doping Ag-NPs into the active layer. As is shown in Table 4.2 the 10 nm and 30 nm doped cells achieved the highest average PCE of 2.64%, while the 5 nm doped cells gave the highest maximum PCE of 2.90%.

	PCE (%)	PCE _{Max} (%)	FF	J _{SC} (mA/cm ²)	V _{OC} (V)	J _{Max} (mA/cm ²)	V _{Max} (V)
Control	2.40		0.574	7.2	0.60	7.2	0.46
5 nm Ag-NP Cells	2.53	2.90	0.507	7.7	0.65	7.7	0.47
10 nm Ag-NP Cells	2.64	2.88	0.608	7.1	0.61	7.1	0.48
20 nm Ag-NP Cells	2.45	2.85	0.593	6.5	0.60	6.5	0.50
30 nm Ag-NP Cells	2.64	2.75	0.612	6.7	0.65	6.7	0.53

Table 4.2: Table of results for ITO/PEDOT:PSS/P3HT:PCBM:Ag-NP /Al cells.

These improvements to the PCE of the devices is likely the result of increased light absorption within the devices. The increased absorption is probably the result of enhanced scattering and light trapping due to the plasmonic properties of the Ag-NPs, which would be consistent with the previous experiments. Additionally, in similar experiments using gold nanoparticles, Xie *et al.* observed that the LSPR of gold nanoparticles excited by light caused dipoles to be generated within the nanoparticles. These dipoles combined with the strong near field of the LSPR distributes throughout the active layer and directly enhances light absorption [22]. In all likelihood, the Ag-NPs exhibit similar properties to their gold counterparts.

Additionally, the improvements to the FF in the 10, 20, and 30 nm Ag-NP doped cells is most likely due to increased hole mobility within the active layer of the devices. This increase in hole mobility would balance out the electron and hole mobilities within the devices allowing more balanced charge transport and thus improving the FF. Such an increase in hole mobility would remain consistent with previous works completed using gold nanoparticles [22].

Furthermore the fluctuations for the J_{SC} , V_{OC} , J_{Max} , and V_{Max} are, in all likelihood, the result of normal fluctuations within the devices.

4.2.3 ITO/PEDOT:PSS/Ag-NP/P3HT:PCBM/Al Cells

The addition of Ag-NPs between the PEDOT:PSS buffer layer and the P3HT:PCBM active layer caused an overall decline in the performance of the respective devices.

Fabricating the OSCs with 5 nm Ag-NPs between the buffer and active layers resulted in an average PCE of 1.70% which was a decrease of 29% as compared to the control devices. Furthermore the maximum PCE obtained was 2.20% which was 8.3% lower than the average PCE of the control cells. A representative J-V curve for

these OSCs is shown in Figure 4.11.

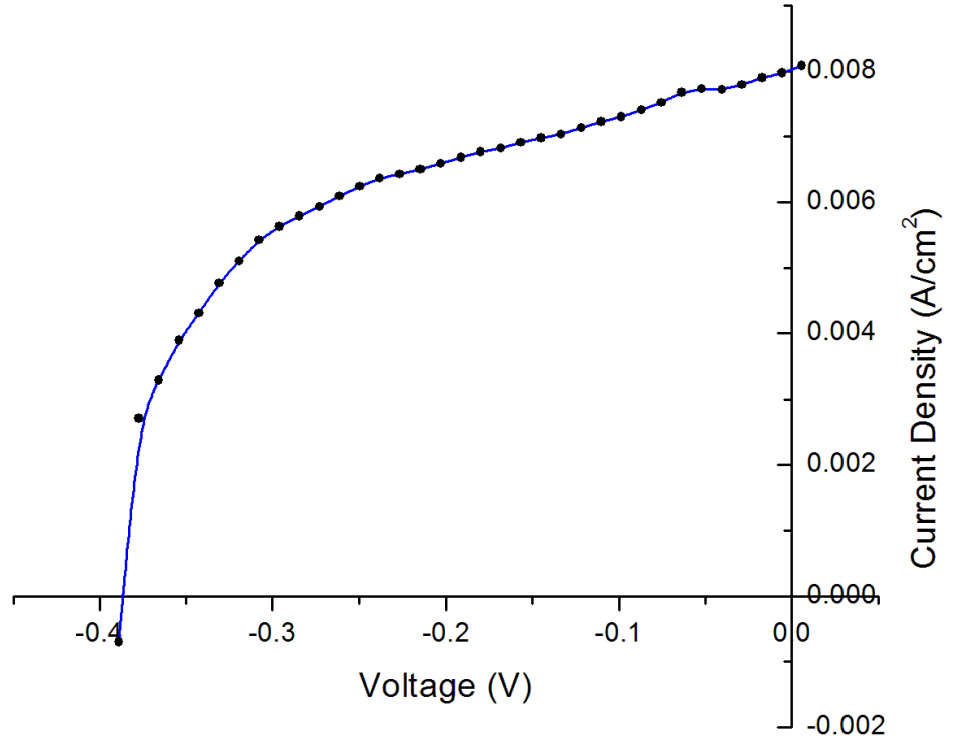


Figure 4.11: J-V curve for 5 nm samples, with structure of ITO/PEDOT:PSS/Ag-NP/P3HT:PCBM/Al.

The FF, J_{SC} , and J_{Max} were 0.590, 7.4 mA/cm², and 7.4 mA/cm² respectively which corresponded to an improvement of 2.8% for each parameter. On the other hand, the V_{OC} and V_{Max} were 0.42 V and 0.32 V, which corresponded to a decrease of 30% as compared to the same parameters for the control devices.

The devices prepared using 10 nm Ag-NPs once again resulted in a decrease in both the average PCE and the maximum PCE of the devices. The average PCE

being 1.60% and the maximum being 1.80% represented decreases of 33% and 25% respectively. Additionally, the average FF of 0.535 was a deterioration of 6.8%. A J-V curve for these 10 nm Ag-NP cells is shown in Figure 4.12.

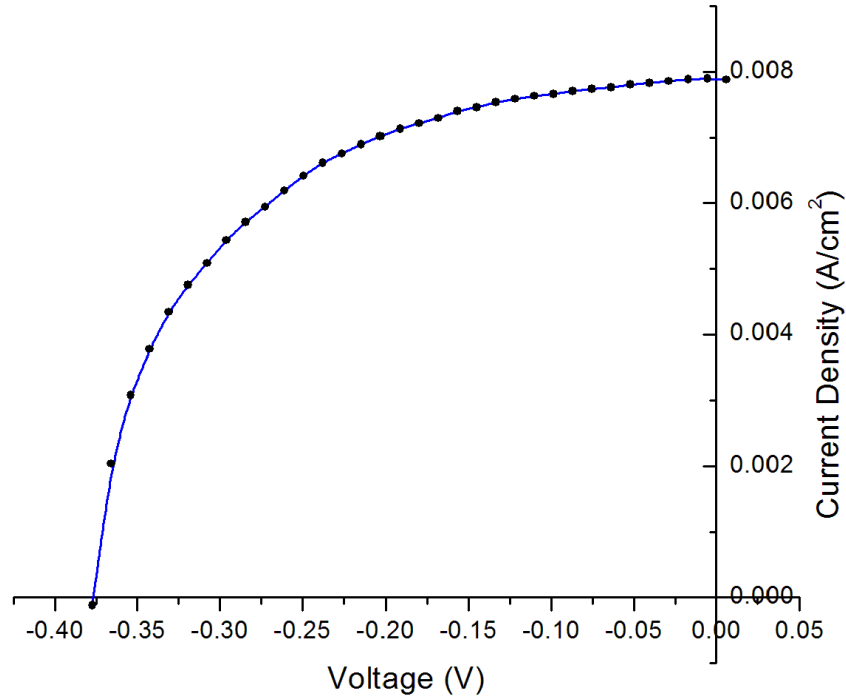


Figure 4.12: J-V curve for 10 nm samples, with structure of ITO/PEDOT:PSS/Ag-NP/P3HT:PCBM/Al.

Furthermore, the J_{SC} , V_{OC} , J_{Max} , and V_{Max} all demonstrated a decrease as compared to their corresponding values for the control devices. Specifically, the J_{SC} and J_{Max} both being 6.4 mA/cm² gave a decrease of 11%, while the V_{OC} and V_{Max} were 0.44 V and 0.33 V respectively, which corresponded with decreases of 27% and 28% as compared to the control devices.

Cells fabricated with 20 nm Ag-NPs also had an overall poor performance when

compared to that of the control devices. Specifically, the average PCE, maximum PCE, and average FF of these cells all gave deteriorated values as compared to the control cells. Moreover the average PCE of 1.63%, maximum PCE of 1.98%, and average FF of 0.532 gave decreases of 32%, 18%, and 7.3% respectively.

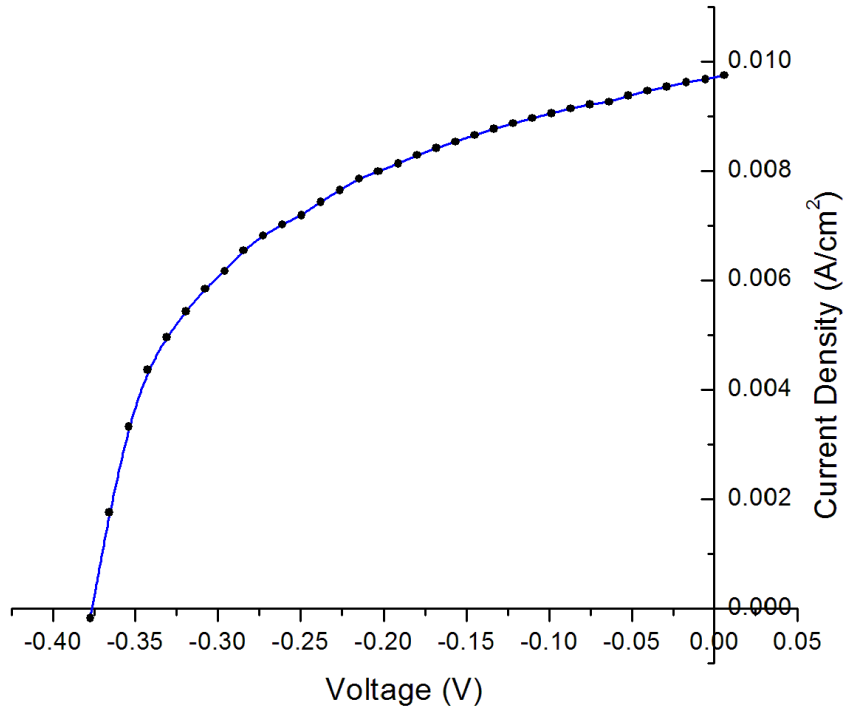


Figure 4.13: J-V curve for 20 nm samples, with structure of ITO/PEDOT:PSS/Ag-NP/P3HT:PCBM/Al.

The J-V curve shown in Figure 4.13 was taken from one of the experiments conducted on the 20 nm Ag-NP devices. It is quite clear to see from Table 4.3 that the V_{OC} and V_{Max} for these devices is significantly decreased from that of the control samples. Specifically the average V_{OC} and V_{Max} of 0.42 V and 0.31 V represented decreases of 30% and 33%. There was, however, an increase of 8.3% in both the J_{SC}

and J_{Max} , giving 7.8 mA/cm² for both parameters.

Using 30 nm Ag-NPs resulted in the lowest performance in all parameters during these tests, specifically the average PCE of 0.88% and maximum PCE of 0.90%. These values were a decrease of approximately 63% as compared to the PCE of the control cells. Additionally the FF was 0.492 which was a decrease of 14%, and a representative J-V curve for these cells is presented in Figure 4.14.

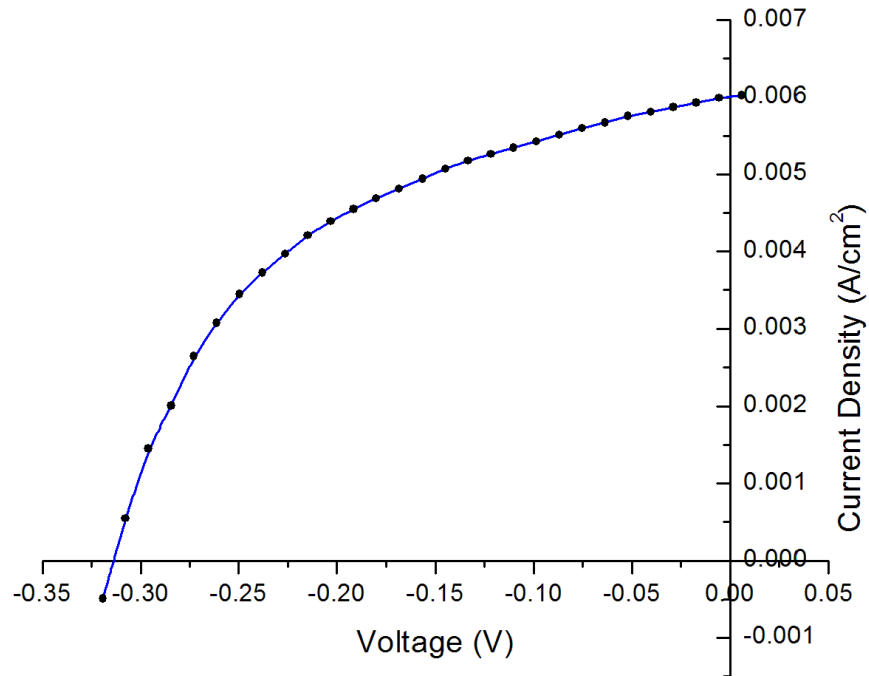


Figure 4.14: J-V curve for 30 nm samples, with structure of ITO/PEDOT:PSS/Ag-NP/P3HT:PCBM/Al.

Additionally the J_{SC} , V_{OC} , J_{Max} , and V_{Max} all demonstrated decreases in value as compared to the control cells. The J_{SC} of 6.0 mA/cm², V_{OC} of 0.31 V, J_{Max} of 6.0 mA/cm², and V_{Max} of 0.21 V were decreases of 17%, 48%, 17%, and 54% respectively.

As is shown in Table 4.3, there was an overall deterioration in device performance for all of the cells prepared with structure ITO/PEDOT:PSS/Ag-NP/P3HT:PCBM/Al. One reason for the decreased performance is likely a slight misalignment of the energy levels of the active layer materials and the work function of the anodic buffer layer.

The addition of the Ag-NPs onto the PEDOT:PSS results in a changed alignment between the energy levels and the work function of the Ag as compared to the PEDOT:PSS at the points of contact between the Ag and the P3HT:PCBM. The changed alignment could result in decreased extraction of electrons from the active layer to the Ag-NPs and thus onto the electrode, the result would therefore be a lowering of the overall device performance.

By spin coating the Ag-NPs from an aqueous solution, it is possible that some water remains on top of the PEDOT:PSS even after the annealing process. It is likely that this remaining water could form a thin film on the PEDOT:PSS, thus decreasing the conductivity between the active layer and the PEDOT:PSS/Ag-NP layer. Such a decrease in conductivity would severely limit charge transport and therefore result in a significantly decreased device performance.

Additionally, considering the rate of degradation of PEDOT:PSS due to humidity, it is likely that spin coating the Ag-NPs from an aqueous solution onto the PEDOT:PSS causes a significant level of deterioration in the PEDOT:PSS layer. Considering that Spyropoulos *et al.* achieved a PCE improvement of 50% by spin coating Ag-NPs from an ethanol solution and using a nearly indistinguishable device configuration from the one used in these experiments, it is probable that the degradation of the PEDOT:PSS layer due to the aqueous Ag-NP solution is the reason for the poor performance of these devices [74].

	PCE (%)	PCE _{Max} (%)	FF	J _{SC} (mA/cm ²)	V _{OC} (V)	J _{Max} (mA/cm ²)	V _{Max} (V)
Control	2.40		0.574	7.2	0.60	7.2	0.46
5 nm Ag-NP Cells	1.70	2.20	0.507	7.4	0.42	7.4	0.32
10 nm Ag-NP Cells	1.60	1.80	0.608	6.4	0.44	6.4	0.33
20 nm Ag-NP Cells	1.63	1.98	0.593	7.8	0.42	7.8	0.31
30 nm Ag-NP Cells	0.88	0.90	0.612	6.0	0.31	6.0	0.21

Table 4.3: Table of results for ITO/PEDOT:PSS/Ag-NP/P3HT:PCBM/Al cells.

4.2.4 ITO/PEDOT:PSS:Ag-NP/P3HT:PCBM/Al Cells

The final set of experiments conducted using the Ag-NPs examined the effectiveness of the different sizes of Ag-NPs when doped into the PEDOT:PSS buffer layer. The result of these experiments was an overall improvement in the performance of these OSCs.

The addition of the 5 nm Ag-NPs improved nearly every performance aspect of the tested devices. Of specific interest is the 8.8% and 14% improvements in the average and maximum PCEs which were 2.61% and 2.73% respectively. The FF also improved by 4.5% to 0.600, and a J-V curve from these tests is demonstrated in Figure 4.15.

Additionally, the J_{SC} and J_{Max} were both 7.5 mA/cm² which was an improvement of 4.2% over their counterparts for the control devices. Furthermore, the V_{OC} remained unchanged from that of the control samples at 0.60 V, and the V_{Max} of 0.45 V only suffered a 2% decrease from the corresponding value of the control devices.

Substituting 10 nm Ag-NPs instead of the 5 nm Ag-NPs also resulted in an improvement to the average and maximum PCE of the devices. The average PCE of 2.57% and the maximum PCE of 2.70% represented improvements of 7.1% and 13%. The FF for these devices was 0.573 which is only a fraction of a percent less than that of the control samples and is, therefore, essentially unchanged from that of the control cells.

Figure 4.16 shows a J-V curve taken from these tests, and the improvements in the V_{OC} are easy to see in this example. Specifically, the average V_{OC} improved by 5% to 0.63 V, whereas the average J_{SC} and J_{Max} improved by 1.4% to 7.3 mA/cm². However, the V_{Max} remained unchanged at 0.46 V from that of the control devices.

Improvements in PCE were also observed through the application of the 20 nm

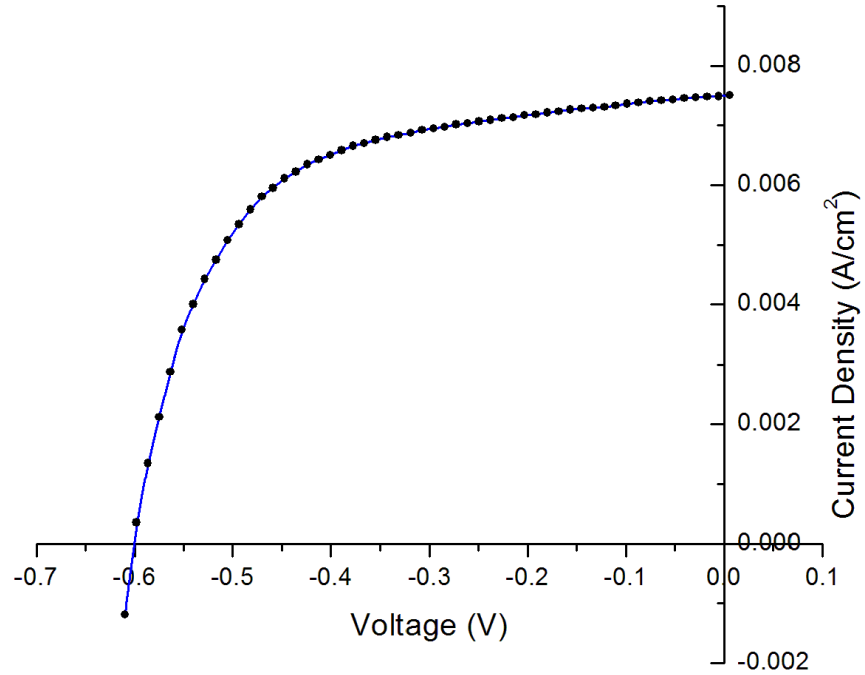


Figure 4.15: J-V curve for 5 nm samples, with structure of ITO/PEDOT:PSS:Ag-NP/P3HT:PCBM/Al.

Ag-NPs doped PEDOT:PSS buffer layer. In fact, the average PCE of 2.53% and the maximum PCE of 2.64% were improvements of 5.4% and 10% respectively over the PCE of the control samples. There was, however, a 7.8% deterioration in the average FF of the devices resulting in a FF of 0.529. A sample J-V curve for these 20 nm Ag-NP doped cells is demonstrated in Figure 4.17.

Additionally, as is demonstrated in Table 4.4, the J_{SC} and J_{Max} are 7.1 mA/cm² and 7.0 mA/cm² respectively, which are slight decreases as compared to the control cells. Specifically, the J_{SC} is 1.4% lower and the J_{Max} is 2.8% lower than that of the control samples. The V_{OC} and V_{Max} however are both improvements over the control

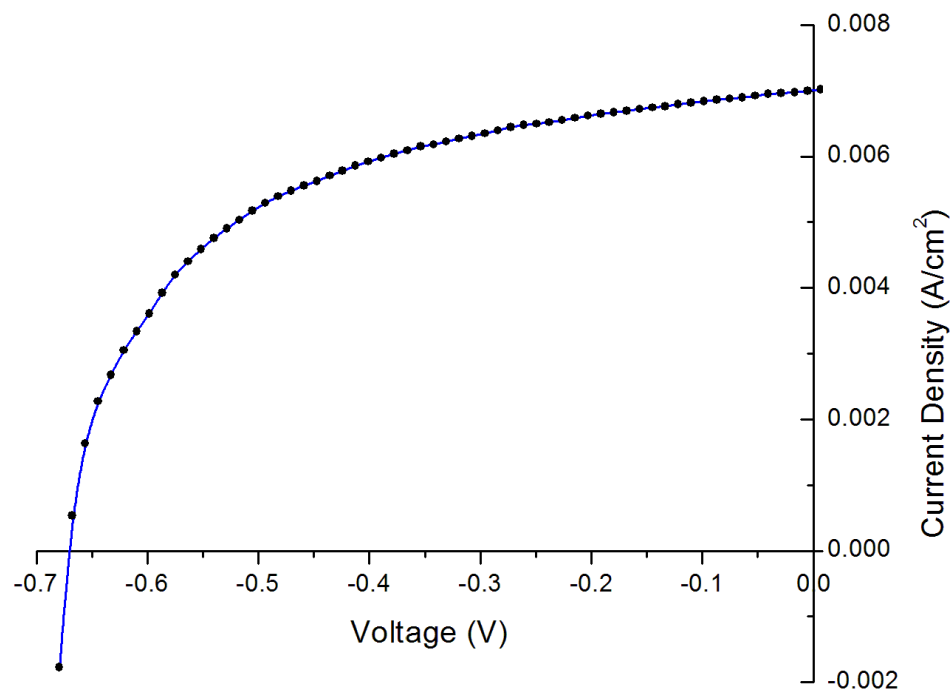


Figure 4.16: J-V curve for 10 nm samples, with structure of ITO/PEDOT:PSS:Ag-NP/P3HT:PCBM/Al.

devices, their values being 0.63 V and 0.47 V respectively. These voltages correspond to improvements of 5% and 2.2% respectively as compared to the corresponding control sample values.

Finally, the cells with 30 nm Ag-NP doped PEDOT:PSS were tested and their results, which are presented in Table 4.4, were remarkably similar to those of the previously examined 20 nm Ag-NP doped cells. Specifically, the average PCE was once again 2.53%, while the maximum PCE was 2.62%, these represented an improvement of 5.4% and 9.2% respectively as compare to the control samples. Additionally the FF was 0.532, which was 7.3% lower than that of the control devices.

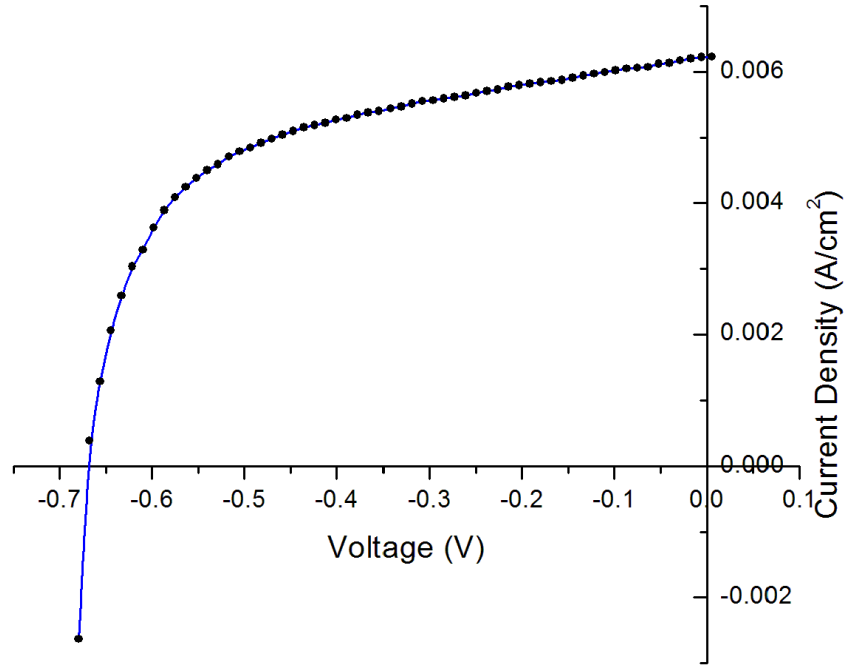


Figure 4.17: J-V curve for 20 nm samples, with structure of ITO/PEDOT:PSS:Ag-NP/P3HT:PCBM/Al.

The average J_{SC} , V_{OC} , J_{Max} , and V_{Max} for these devices are also very similar to that of the 20 nm Ag-NP doped cells. Specifically, the V_{OC} and V_{Max} of 0.63 V and 0.47 V are the same for 20 and 30 nm Ag-NP doped PEDOT:PSS devices and as previously stated are improvements of 5% and 2.2%. Moreover, the J_{SC} and J_{Max} are 7.2 mA/cm², which is unchanged from that of the control devices. Figure 4.18 demonstrates a J-V curve taken from the 30 nm Ag-NP doped experiments with values very close to the average values calculated from the tested samples.

Overall, the doping of Ag-NPs into the PEDOT:PSS layer of these OSCs resulted in an improvement to their performance. Specifically, improvements of 5.4% to 8.8%

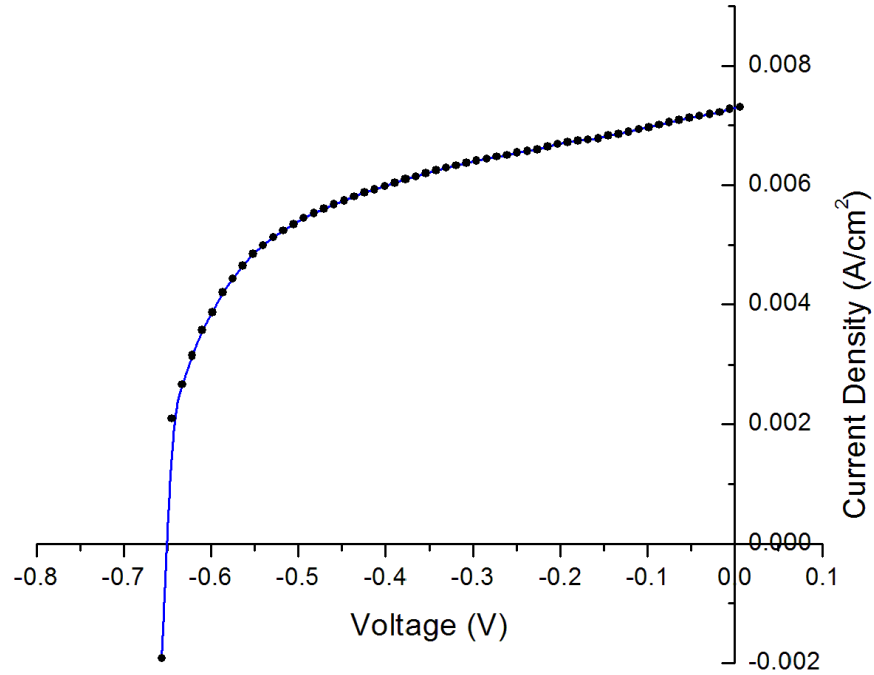


Figure 4.18: J-V curve for 30 nm samples, with structure of ITO/PEDOT:PSS:Ag-NP/P3HT:PCBM/Al.

in the average PCE, and 9.2% to 14% in maximum PCE were observed for these devices. Table 4.4 shows that while the performance improved for each of the Ag-NP sizes tested, the smaller 5 nm nanoparticles resulted in the highest performance increase.

The improved efficiency in the 5 and 10 nm Ag-NP cells is likely partially due to the increased J_{SC} and J_{Max} , as well as the improved FF for the 5 nm devices. These improvements are likely the result of enhanced absorption within the cells due to increased scattering due to the LSPR of the Ag-NPs [64]. This improved scattering would increase light trapping within the devices, thus allowing more light

	PCE (%)	PCE _{Max} (%)	FF	J _{SC} (mA/cm ²)	V _{OC} (V)	J _{Max} (mA/cm ²)	V _{Max} (V)
Control	2.40		0.574	7.2	0.60	7.2	0.46
5 nm Ag-NP Cells	2.61	2.73	0.600	7.5	0.60	7.5	0.45
10 nm Ag-NP Cells	2.57	2.70	0.573	7.3	0.63	7.3	0.46
20 nm Ag-NP Cells	2.53	2.64	0.529	7.1	0.63	7.0	0.47
30 nm Ag-NP Cells	2.53	2.62	0.532	7.2	0.63	7.2	0.47

Table 4.4: Table of results for ITO/PEDOT:PSS:Ag-NP/P3HT:PCBM/Al cells.

to be absorbed within the cells [25].

On the other hand, the increased performance of the 20 and 30 nm Ag-NP doped cells is most likely partially due to the improved V_{OC} and V_{Max} for these cells. While the plasmonic properties of these Ag-NPs likely improves light scattering and absorption within the cells, such improvements usually only improve the J_{SC} , J_{Max} , and FF [22, 25, 64]. Therefore, these improvements to V_{OC} and V_{Max} are most likely result of slight improvements to conductivity and resistivity.

4.3 Incorporation of Transition Metal Oxides into Organic Solar Cells

Cells consisting of the transition metal oxide CdO spin coated at 1500, 2500, and 3500 rpm onto the ITO as a substitute for PEDOT:PSS were tested. Then the cells with the inverted structures of ITO/TiO₂/P3HT:PCBM/CdO/Al and ITO/TiO₂/P3HT:PCBM/MoO₃/Al were prepared and tested.

Once again a minimum of three substrates were prepared and tested for each of the desired CdO spin coating speeds as well as inverted cell structures.

4.3.1 ITO/CdO/P3HT:PCBM/Al Cells

After fabrication, the cells with 1500 and 2500 rpm spin coated CdO were exposed to the solar simulator and their J-V curves were recorded and examined. Despite numerous repeated attempts these cells produced no viable results with their respective J-V curves giving either no result at all, or that of a short circuit. Where no J-V curve was obtained, this was a result of extremely poor or no conductivity between the layers of the cells, thus preventing the passage of electricity and resulting in no

J-V curve. For the cells where a J-V curve for a short circuit was obtained, this is the most likely the result of small pinholes in the layers allowing electricity to arc between the anode and cathode.

The J-V curve for a short circuit is the same as that for running the source-meter with the positive and negative leads connected to one another.

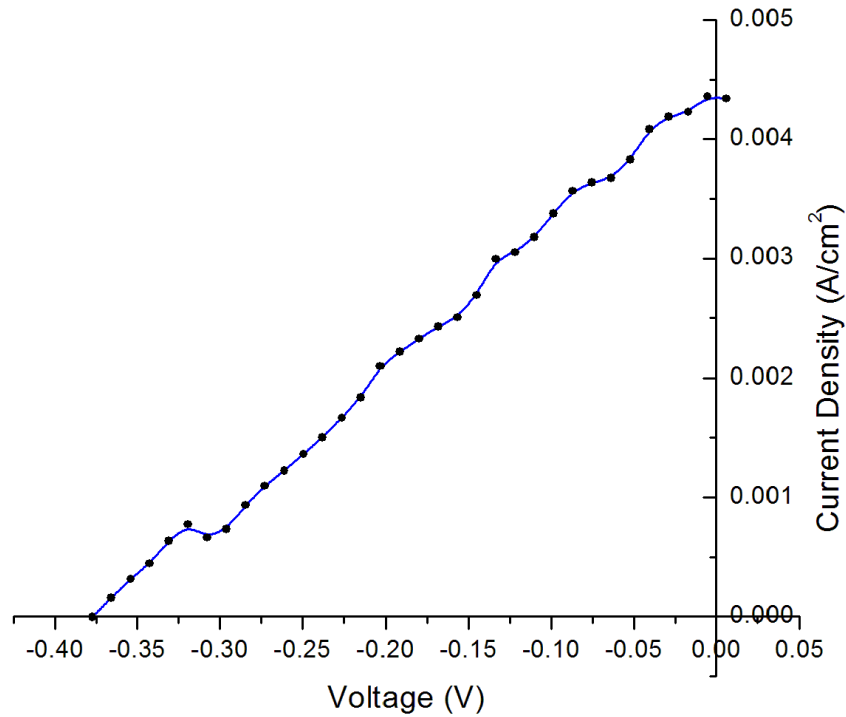


Figure 4.19: J-V curve for CdO samples spin coated at 3500 rpm, with structure of ITO/CdO/P3HT:PCBM/Al.

Spin coating at 3500 rpm on the other hand did produce a small number of viable results. While the overall performance of the cells was exceptionally poor, using CdO as an anodic buffer layer did achieve an average PCE of 0.25% and a maximum PCE of 0.43%. These results were a 90% and 82% decrease as compared to the control cells

prepared using PEDOT:PSS. The J-V curve for the cell which gave the maximum PCE is shown in Figure 4.19, and Table 4.5 gives the measured values for the J_{SC} , V_{OC} , J_{Max} , and V_{Max} .

The poor performance of CdO to act as a substitute for PEDOT:PSS as a buffer layer between the P3HT:PCBM and the ITO is most likely a result of CdO's lower conductivity as compared to PEDOT:PSS. This decrease in conductivity results in a deteriorated charge transport from the active layer to the electrode and thus reduces the device performance.

4.3.2 ITO/TiO₂/P3HT:PCBM/CdO/Al and ITO/TiO₂/P3HT:PCBM/MoO₃/Al Cells

The inverted solar cell structures of ITO/TiO₂/P3HT:PCBM/MoO₃/Al and ITO/TiO₂/P3HT:PCBM/CdO/Al were both exposed to solar simulation with the resulting J-V curves being recorded. Unfortunately the highest observed PCE for the ITO/TiO₂/P3HT:PCBM/MoO₃/Al control cells was 0.65% which was significantly lower than expected.

Previous works such as those by Li *et al.* [67], Loiudice *et al.* [75], and Tao *et al.* [76], have shown that inverted OSCs with the same structure as those chosen for these experiments should have a PCE equal to or greater than the 2.40% of our control samples. Huang *et al.* have previously given a PCE of 3.65% for the given inverted structure [77].

The low PCE achieved for our inverted cells is most likely due to a lack of optimization of the layer thicknesses of both the TiO₂ and the MoO₃. The effect of the thickness of the TiO₂ and MoO₃ layers is demonstrated by Sun *et al.* who demonstrated an improvement of ~100% depending on TiO₂ thickness [78], and Wang *et*

	PCE (%)	PCE _{Max} (%)	FF	J _{SC} (mA/cm ²)	V _{OC} (V)	J _{Max} (mA/cm ²)	V _{Max} (V)
Control	2.40		0.574	7.2	0.60	7.2	0.46
3500 rpm CdO	0.25	0.43	0.255	3.1	0.39	3.1	0.20

Table 4.5: Table of results for ITO/CdO/P3HT:PCBM/Al cells.

al. who demonstrated an over 500% improvement in PCE with a change of just 5 nm in MoO₃ thickness [79].

Additionally, the inverted cells prepared using CdO also failed to produce any viable results. Much like for the standard structure OSCs using CdO in the previous section, the recorded J-V curves either yielded no result at all, or that of a short circuit. The reasons for the failure of these cells is once again likely due to CdO's slightly lower conductivity as compared to MoO₃ as well as the unoptimized layer thickness of the TiO₂ buffer layers.

Unfortunately, the process of optimizing the layer thickness for the TiO₂ and MoO₃ layers is a fairly intensive and time consuming process. As a result, it was necessary to abandon further study in this area due to the required time constraints of this project.

Chapter 5

Conclusion

5.1 Summary

The original goal of this project was to improve the performance of organic solar cells through the addition of 5, 10, 20, and 30 nm silver nanoparticles; additionally the transition metal oxide cadmium oxide was tested to determine its potential for use as a buffer layer in OSCs. Furthermore, the effect of the 5, 10, 20, and 30 nm Ag-NPs in each of the desired structural configurations of the OSCs was examined.

These experiments were completed through the fabrication and testing (under simulated AM 1.5G irradiation) of solar cells with structures of ITO/Ag-NP/PEDOT:PSS/P3HT:PCBM/Al, ITO/PEDOT:PSS/P3HT:PCBM:Ag-NP/Al, ITO/PEDOT:PSS/Ag-NP/P3HT:PCBM/Al, ITO/PEDOT:PSS:Ag-NP/P3HT:PCBM/Al, ITO/CdO/P3HT:PCBM/Al, and ITO/TiO₂/PCBM:P3HT/CdO/Al. The results of these tests were then compared with the appropriate control cell whose structure was either ITO/PEDOT:PSS/P3HT:PCBM/Al or ITO/TiO₂/P3HT:PCBM/MoO₃/Al.

5.1.1 Silver Nanoparticle Cells

The addition of the Ag-NPs between the ITO substrate and the PEDOT:PSS buffer layer gave an improvement to power conversion efficiency of the device regardless of the particle sizes tested. The use of 5 nm Ag-NPs produced the most significant improvement (8.3%) in average PCE and the use of 10 nm Ag-NPs provided the largest improvement (20%) in maximum PCE. Additionally, all four sizes of Ag-NPs improved the fill factor of the devices, and the use of the 30 nm Ag-NPs resulted in the largest improvement at 16%.

The overall improvement in device performance for this configuration is a result of the plasmonic properties of the Ag-NPs improving both light scattering and trapping within the devices. These improvements enhance the absorption with the devices and thus increases the amount of light energy which is converted to electricity. Additionally, slight decreases in series resistance due to the Ag-NPs results in an improved FF which contributes to an increased PCE.

Doping the Ag-NPs into the P3HT:PCBM active layer improved device performance for all four sizes of Ag-NPs, with the 10 and 30 nm nanoparticles resulting in the largest increase of 10% in average PCE. Furthermore the 5 nm Ag-NPs gave the largest increase in the maximum PCE of 21% and the 30 nm nanoparticles increased the FF the most, improving it by 6.6%.

The improvement of the performance of the devices with the Ag-NPs doped into the active layer is likely the result of improved electron mobility within the active layer increasing the FF of the devices. Additionally, the plasmonic properties of the Ag-NPs enhances both light scattering and trapping which results in higher light absorption within the cells.

While adding Ag-NPs between the PEDOT:PSS and P3HT:PCBM failed to im-

prove the overall performance of the devices, this is most likely the result of degradation of the PEDOT:PSS layer due to the introduction of moisture from the aqueous Ag-NP solution. Such deterioration of the PEDOT:PSS layer would decrease the conductivity between both the ITO and P3HT:PCBM layers and the PEDOT:PSS, this would result in decreased charge transport and thus a decreased PCE for the devices.

The OSCs fabricated with Ag-NPs doped into the PEDOT:PSS layer improved the PCE of the devices for all four sizes of nanoparticles. Furthermore, the addition of the 5 nm Ag-NPs gave the largest improvements of 8.8% and 14% respectively to both the average PCE and maximum PCE. Moreover, it was the only Ag-NP size to increase the FF of the device with an improvement of 4.5%.

For these cells the enhancements to device performance and FF are likely the result of an improvement in electron transfer within the PEDOT:PSS layer and a decrease in the series resistance within the cell. Once again, the plasmonic properties of the Ag-NPs likely enhances the light trapping and thus absorption within the cells.

Overall, the addition of Ag-NPs into the P3HT:PCBM based OSCs improved the device performance in all but one of the tested structures. Moreover, the addition of 5 nm Ag-NPs often resulted in the largest improvement in device PCE, however the addition of 10 nm particles often produced device performances that were marginally less than that of the 5 nm Ag-NPs.

5.1.2 Cadmium Oxide Cells

While the use of CdO as a buffer layer for OSCs failed to achieve a PCE similar to or greater than that of OSCs using PEDOT:PSS, it did demonstrate that it is possible to fabricate an organic solar cell using CdO. While the overall device performance

was poor in every aspect, the fact that the device provided a valid J-V curve and result demonstrates that there may still be potential for improvement.

5.2 Future Work

It would be exceptionally valuable to further examine the effects of the Ag-NPs on the optical absorption and transmission coefficients within OSCs. This information could potentially be used to tailor a device for an application such as power generating windows. In such an application it would be desirable to allow the transmission of visible light but to absorb both infrared and ultraviolet light so that their energy could be converted into electricity.

It would also be prudent to examine the effects of Ag-NPs on OSCs with different device structures such as those with an active layer comprised of materials other than P3HT:PCBM. Additionally, the use of Ag-NPs as a conducting or buffer layer between cells in a tandem or multi-junction cell arrangement could also prove to be beneficial.

Other methods of applying the Ag-NPs should also be examined; while the application of the nanoparticles through an aqueous solution is convenient for spin coating, the additional moisture will likely cause quicker deterioration of the devices and thus hamper their long-term performance. By applying or doping the Ag-NPs directly where they are required using alternate application methods, there could be a significant increase in the device longevity as well as an immediate improvement in device performance.

While it is likely that the plasmonic resonance peak for the 5 and 10 nm Ag-NPs aligns more closely with the peak of the AM 1.5G irradiation than that of the 20 and 30 nm Ag-NPs, it would be beneficial to confirm this fact. Such confirmation would

identify if there are other factors benefiting the 5 and 10 nm particles as opposed to the 20 and 30 nm particles. Such information has the potential to provide insights that would be beneficial for the creation of new materials that would further improve OSC performance.

Additionally, more study into the use of CdO for OSCs is necessary. Properties such as absorption, transmission, and conduction should be examined to further determine whether CdO is in fact suitable for use in OSCs. Furthermore, should CdO prove to be suitable material, the deposition method and the thickness of the CdO layer will both need to be optimized in order to achieve the maximum possible device performance.

Bibliography

- [1] Dieter Wöhrle and Dieter Meissner. Organic solar cells. *Advanced Materials*, 3(3):129–138, 1991.
- [2] C. B. Hatfield. Oil back on the global agenda. *Nature*, 387:121, 1997.
- [3] International Energy Agency. 2014 key world energy statistics. 2014.
- [4] Intergovernmental Panel of Climate Change (IPCC). Second assessment report - climate change 1995. 1995.
- [5] Ian Gynther, Natalie Waller, L. K.-P Leung (Luke K.-P.), Queensland. Department of Environment, and Heritage Protection. Confirmation of the extinction of the bramble cay melomys melomys rubicola on bramble cay, torres strait : results and conclusions from a comprehensive survey in August September 2014. 2016.
- [6] Hui Huang and Jinsong Huang. *Organic and Hybrid Solar Cells*. Series on Properties of Semiconductor Materials. Springer International Publishing, 2014.
- [7] Yulia Galagan, Michael G. Debije, and Paul W. M. Blom. Semitransparent organic solar cells with organic wavelength dependent reflectors. *Applied Physics Letters*, 98(4), 2011.

- [8] Lance Frazer. Organic electronics: a cleaner substitute for silicon. *Environmental Health Perspectives*, 111:A288 – A291, 2003.
- [9] The Editors of Encyclopaedia Britannica. Photovoltaic effect. <http://www.britannica.com/science/photovoltaic-effect>, 2015. [Online; accessed 2015-06-12].
- [10] R. McNeill, R. Siudak, J. H. Wardlaw, and D. E. Weiss. Electronic conduction in polymers. I. the chemical structure of polypyrrole. *Australian Journal of Chemistry*, 16:1056–1075, 1963.
- [11] Gang Li, Vishal Shrotriya, Yan Yao, and Yang Yang. Investigation of annealing effects and film thickness dependence of polymer solar cells based on poly(3-hexylthiophene). *Journal of Applied Physics*, 98(4), 2005.
- [12] Rafael Gómez, José L. Segura, and Nazario Martín. Highly efficient light-harvesting organofullerenes. *Organic Letters*, 7(4):717–720, 2005. PMID: 15704933.
- [13] Minh Trung Dang, Lionel Hirsch, and Guillaume Wantz. P3HT:PCBM, best seller in polymer photovoltaic research. *Advanced Materials*, 23(31):3597–3602, 2011.
- [14] Nobel Media. The nobel prize in chemistry 2000. http://www.nobelprize.org/nobel_prizes/chemistry/laureates/2000/, 2000. [Online; accessed 2016-08-10].
- [15] M. D. Archer and R. Hill. *Clean Electricity from Photovoltaics*. Series on photo-conversion of solar energy. Imperial College Press, London, UK, 2 edition, 2001.

- [16] Frank Dimroth, Matthias Grave, Paul Beutel, Ulrich Fiedeler, Christian Karcher, Thomas N. D. Tibbits, Eduard Oliva, Gerald Siefer, Michael Schachtner, Alexander Wekkeli, Andreas W. Bett, Rainer Krause, Matteo Piccin, Nicolas Blanc, Charlotte Drazek, Eric Guiot, Bruno Ghyselen, Thierry Salvetat, Aurlie Tauzin, Thomas Signamarcheix, Anja Dobrich, Thomas Hannappel, and Klaus Schwarzburg. Wafer bonded four-junction GaInP/GaAs//GaInAsP/GaInAs concentrator solar cells with 44.7% efficiency. *Progress in Photovoltaics: Research and Applications*, 22(3):277–282, 2014. PIP-13-265.R1.
- [17] Jingbi You, Letian Dou, Ken Yoshimura, Takehito Kato, Kenichiro Ohya, Tom Moriarty, Keith Emery, Chun-Chao Chen, Jing Gao, Gang Li, et al. A polymer tandem solar cell with 10.6% power conversion efficiency. *Nature communications*, 4:1446, 2013.
- [18] Zhong Zheng, Shaoqing Zhang, Maojie Zhang, Kang Zhao, Long Ye, Yu Chen, Bei Yang, and Jianhui Hou. Highly efficient tandem polymer solar cells with a photovoltaic response in the visible light range. *Advanced Materials*, 27(7):1189–1194, 2015.
- [19] Yong Hyun Kim, Christoph Sachse, Martin Hermenau, Karsten Fehse, Moritz Riede, Lars Mller-Meskamp, and Karl Leo. Improved efficiency and lifetime in small molecule organic solar cells with optimized conductive polymer electrodes. *Applied Physics Letters*, 99(11), 2011.
- [20] Marco Notarianni, Kristy Vernon, Alison Chou, Muhsen Aljada, Jinzhang Liu, and Nunzio Motta. Plasmonic effect of gold nanoparticles in organic solar cells. *Solar Energy*, 106:23 – 37, 2014. Third and Fourth Generation Solar Cells.

- [21] Seung Joo Lee, Jae-Yeon Kim, Abd. Rashid bin Mohd Yusoff, and Jin Jang. Plasmonic organic solar cell employing Au NP:PEDOT:PSS doped rGO. *RSC Adv.*, 5:23892–23899, 2015.
- [22] Feng-Xian Xie, Wallace C. H. Choy, Charlie C. D. Wang, Wei E. I. Sha, and Dixon D. S. Fung. Improving the efficiency of polymer solar cells by incorporating gold nanoparticles into all polymer layers. *Applied Physics Letters*, 99(15):–, 2011.
- [23] Shiva Shahin, Palash Gangopadhyay, and Robert A. Norwood. Ultrathin organic bulk heterojunction solar cells: Plasmon enhanced performance using au nanoparticles. *Applied Physics Letters*, 101(5):1–4, 2012.
- [24] N. Kalfagiannis, P. G. Karagiannidis, C. Pitsalidis, N. T. Panagiotopoulos, C. Gravalidis, S. Kassavetis, P. Patsalas, and S. Logothetidis. Plasmonic silver nanoparticles for improved organic solar cells. *Solar Energy Materials and Solar Cells*, 104:165 – 174, 2012.
- [25] K. S. Hamdan, S. M. Abdullah, K. Sulaiman, and R. Zakaria. Effects of silver nanoparticles towards the efficiency of organic solar cells. *Applied Physics A*, 115(1):63–68, 2014.
- [26] Johannes Godt, Franziska Scheidig, Christian Gosse-Siestrup, Vera Esche, Paul Brandenburg, Andrea Reich, and David A. Groneberg. The toxicity of cadmium and resulting hazards for human health. *Journal of Occupational Medicine and Toxicology*, 1:22, 2016.
- [27] W. W. Anderson and Y. G. Chai. Becquerel effect solar cell. *Energy Conversion*, 15(3):85 – 94, 1976.

- [28] A. E. Becquerel. Mémoire sur les effets électriques produits sous l'influence des rayons solaires. *Comptes Rendus des Séances Hebdomadaires*, 9:561–567, 1839.
- [29] Richard Williams. Becquerel photovoltaic effect in binary compounds. *The Journal of Chemical Physics*, 32(5):1505–1514, 1960.
- [30] David Kearns and Melvin Calvin. Photovoltaic effect and photoconductivity in laminated organic systems. *The Journal of Chemical Physics*, 29(4):950–951, 1958.
- [31] H. Tang, K. Prasad, R. Sanjins, P. E. Schmid, and F. Lvy. Electrical and optical properties of TiO₂ anatase thin films. *Journal of Applied Physics*, 75(4):2042–2047, 1994.
- [32] Ting Shi, Xiaoguang Zhu, and Guoli Tu. Efficient inverted polymer solar cells based on ultrathin aluminum interlayer modified aluminum-doped zinc oxide electrode. *Applied Physics Letters*, 104(10):1–4, 2014.
- [33] Jo-Lin Lan, Zhiqiang Liang, Yi-Hsun Yang, Fumio S. Ohuchi, Samson A. Jenekhe, and Guozhong Cao. The effect of SrTiO₃:ZnO as cathodic buffer layer for inverted polymer solar cells. *Nano Energy*, 4:140 – 149, 2014.
- [34] Than Zaw Oo, R. Devi Chandra, Natalia Yantara, Rajiv Ramanujam Prabhakar, Lydia H. Wong, Nripan Mathews, and Subodh G. Mhaisalkar. Zinc tin oxide (ZTO) electron transporting buffer layer in inverted organic solar cell. *Organic Electronics*, 13(5):870 – 874, 2012.
- [35] Vishal Shrotriya, Gang Li, Yan Yao, Chih-Wei Chu, and Yang Yang. Transition metal oxides as the buffer layer for polymer photovoltaic cells. *Applied Physics Letters*, 88(7):1–3, 2006.

- [36] Zhan'ao Tan, Deping Qian, Wenqing Zhang, Liangjie Li, Yuqin Ding, Qi Xu, Fuzhi Wang, and Yongfang Li. Efficient and stable polymer solar cells with solution-processed molybdenum oxide interfacial layer. *Journal of Materials Chemistry A*, 1:657–664, 2013.
- [37] Ziyang Hu, Jianjun Zhang, and Ying Zhao. Efficient polymer solar cells based on light-trapping transparent electrodes. *Applied Physics Letters*, 100(10), 2012.
- [38] T. Praveen, K. Shiju, and P. Predeep. Influence of plasma treatment on indium tin oxide electrodes. *Microelectronic Engineering*, 131:8 – 12, 2015.
- [39] C. W. Tang. Twolayer organic photovoltaic cell. *Applied Physics Letters*, 48(2):183–185, 1986.
- [40] Hsing-Ju Wang, Chih-Ping Chen, and Ru-Jong Jeng. Polythiophenes comprising conjugated pendants for polymer solar cells: A review. *Materials*, 7(4):2411, 2014.
- [41] Jean-Michel Nunzi. Organic photovoltaic materials and devices. *Comptes Rendus Physique*, 3(4):523 – 542, 2002.
- [42] S. S. Sookhun, C. A. Bates, J. L. Dunn, and W. Diery. Multiple occupancy of triply degenerate states in icosahedral symmetry. In *Advances in Quantum Chemistry*, volume 44 of *Advances in Quantum Chemistry*, pages 319 – 334. Academic Press, Nottingham, 2003.
- [43] Yu-Xiang Liu, Melissa A. Summers, Shawn R. Scully, and Michael D. McGehee. Resonance energy transfer from organic chromophores to fullerene molecules. *Journal of Applied Physics*, 99(9), 2006.

- [44] Hanying Li, Benjamin C-K. Tee, Judy J. Cha, Yi Cui, Jong Won Chung, Sang Yoon Lee, and Zhenan Bao. High-mobility field-effect transistors from large-area solution-grown aligned C₆₀ single crystals. *Journal of the American Chemical Society*, 134(5):2760–2765, 2012. PMID: 22239604.
- [45] H. Kallmann and M. Silver. *Symposium of Electrical Conductivity in Organic Solids*. Wiley-Interscience, New York, 1961.
- [46] F. Gutmann and L. E. Lyons. *Organic Semiconductors*. Wiley, California, 1967.
- [47] Serap Günes, Helmut Neugebauer, and Niyazi Serdar Sariciftci. Conjugated polymer-based organic solar cells. *Chemical Reviews*, 107(4):1324–1338, 2007. PMID: 17428026.
- [48] Peter Peumans, Aharon Yakimov, and Stephen R. Forrest. Small molecular weight organic thin-film photodetectors and solar cells. *Journal of Applied Physics*, 93(7):3693–3723, 2003.
- [49] Sean E. Shaheen, Christoph J. Brabec, N. Serdar Sariciftci, Franz Padinger, Thomas Fromherz, and Jan C. Hummelen. 2.5 *Applied Physics Letters*, 78(6):841–843, 2001.
- [50] J. M. Kroon, M. M. Wienk, W. J. H. Verhees, and J. C. Hummelen. Accurate efficiency determination and stability studies of conjugated polymer/fullerene solar cells. *Thin Solid Films*, 403-404(7):223–228, Feb 2002. Journal EB 1 25DQ HIN SOLID FILMS.
- [51] P. Peumans and S. R. Forrest. Very-high-efficiency double-heterostructure copper phthalocyanine/C₆₀ photovoltaic cells. *Applied Physics Letters*, 79(1):126–128, 2001.

- [52] Xuanhua Li, Wallace C. H. Choy, Lijun Huo, Fengxian Xie, Wei E. I. Sha, Baofu Ding, Xia Guo, Yongfang Li, Jianhui Hou, Jingbi You, and Yang Yang. Dual plasmonic nanostructures for high performance inverted organic solar cells. *Advanced Materials*, 24(22):3046–3052, 2012.
- [53] Luyao Lu, Zhiqiang Luo, Tao Xu, and Luping Yu. Cooperative plasmonic effect of ag and au nanoparticles on enhancing performance of polymer solar cells. *Nano Letters*, 13(1):59–64, 2013. PMID: 23237567.
- [54] Chun-Chao Chen, Wei-Hsuan Chang, Ken Yoshimura, Kenichiro Ohya, Jingbi You, Jing Gao, Zirou Hong, and Yang Yang. An efficient triple-junction polymer solar cell having a power conversion efficiency exceeding 11%. *Advanced Materials*, 26(32):5670–5677, 2014.
- [55] Kyungkon Kim and David L. Carroll. Roles of Au and Ag nanoparticles in efficiency enhancement of poly(3-octylthiophene)/C60 bulk heterojunction photovoltaic devices. *Applied Physics Letters*, 87(20):1–3, 2005.
- [56] Linfang Qiao, Dan Wang, Lijian Zuo, Yuqian Ye, Jun Qian, Hongzheng Chen, and Sailing He. Localized surface plasmon resonance enhanced organic solar cell with gold nanospheres. *Applied Energy*, 88(3):848 – 852, 2011.
- [57] Ken-Tye Yong, Yudhisthira Sahoo, Mark T. Swihart, and Paras N. Prasad. Synthesis and plasmonic properties of silver and gold nanoshells on polystyrene cores of different size and of goldsilver coreshell nanostructures. *Colloids and Surfaces A: Physicochemical and Engineering Aspects*, 290(13):89 – 105, 2006.
- [58] M. P. de Jong, L. J. van IJzendoorn, and M. J. A. de Voigt. Stability of the interface between indium-tin-oxide and poly(3,4-

- ethylenedioxythiophene)/poly(styrenesulfonate) in polymer light-emitting diodes. *Applied Physics Letters*, 77(14):2255–2257, 2000.
- [59] K. W. Wong, H. L. Yip, Y. Luo, K. Y. Wong, W. M. Lau, K. H. Low, H. F. Chow, Z. Q. Gao, W. L. Yeung, and C. C. Chang. Blocking reactions between indium-tin oxide and poly (3, 4-ethylene dioxythiophene): poly (styrene sulphonate) with a self-assembly monolayer. *Applied physics letters*, 80:2788, 2002.
- [60] T. P. Nguyen and S. A. de Vos. An investigation into the effect of chemical and thermal treatments on the structural changes of poly(3,4-ethylenedioxythiophene)/polystyrenesulfonate and consequences on its use on indium tin oxide substrates. *Applied Surface Science*, 221(14):330 – 339, 2004.
- [61] Jens Meyer, Sami Hamwi, Michael Kröger, Wolfgang Kowalsky, Thomas Riedl, and Antoine Kahn. Transition metal oxides for organic electronics: Energetics, device physics and applications. *Advanced Materials*, 24(40):5408–5427, 2012.
- [62] S. K. Vasheghani Farahani, V. Muoz-Sanjos, J. Ziga-Prez, C. F. McConville, and T. D. Veal. Temperature dependence of the direct bandgap and transport properties of CdO. *Applied Physics Letters*, 102(2):1–4, 2013.
- [63] Qiang Zhou, Zhenguo Ji, BinBin Hu, Chen Chen, Lina Zhao, and Chao Wang. Low resistivity transparent conducting CdO thin films deposited by {DC} reactive magnetron sputtering at room temperature. *Materials Letters*, 61(2):531 – 534, 2007.
- [64] Se-Woong Baek, Jonghyeon Noh, Chun-Ho Lee, BongSoo Kim, Min-Kyo Seo, and Jung-Yong Lee. Plasmonic forward scattering in organic solar cells: A powerful optical engineering method. *Scientific Reports*, 3(1726), 2013.

- [65] Zhixiong Cao, Zhuoying Chen, and Ludovic Escoubas. Optical, structural, and electrical properties of pedot:pss thin films doped with silver nanoprisms. *Opt. Mater. Express*, 4(12):2525–2534, Dec 2014.
- [66] Katarzyna Siuzdak, Mamatimin Abbas, Laurence Vignau, Mlanie Devynck, Galina V. Dubacheva, and Anna Lisowska-Oleksiak. Application of non-metal doped titania for inverted polymer solar cells. *Journal of Applied Physics*, 112(12):1–5, 2012.
- [67] Fumin Li, Chong Chen, Furui Tan, Gentian Yue, Liang Shen, and Weifeng Zhang. A new method to disperse CdS quantum dot-sensitized TiO₂ nanotube arrays into P3HT:PCBM layer for the improvement of efficiency of inverted polymer solar cells. *Nanoscale Research Letters*, 9(1):240, 2014.
- [68] Yanfei Ding. Organic bulk heterojunction solar cells with improved efficiency. 2009.
- [69] C.A. Gueymard, D. Myers, and K. Emery. Proposed reference irradiance spectra for solar energy systems testing. *Solar Energy*, 73(6):443 – 467, 2002.
- [70] Inc. Wolfram Research. *Mathematica*. Wolfram Research, Inc., Champaign, Illinois, Version 10.3 edition, 2015.
- [71] Boyuan Qi and Jizheng Wang. Fill factor in organic solar cells. *Physical Chemistry Chemical Physics*, 15:8972–8982, 2013.
- [72] Woo-Jun Yoon, Kyung-Young Jung, Jiwen Liu, Thirumalai Duraisamy, Rao Revur, Fernando L. Teixeira, Suvankar Sengupta, and Paul R. Berger. Plasmon-enhanced optical absorption and photocurrent in organic bulk heterojunction

- photovoltaic devices using self-assembled layer of silver nanoparticles. *Solar Energy Materials and Solar Cells*, 94(2):128 – 132, 2010.
- [73] Vikas Kumar and Heming Wang. Plasmonic au nanoparticles for enhanced broadband light absorption in inverted organic photovoltaic devices by plasma assisted physical vapour deposition. *Organic Electronics*, 14(2):560 – 568, 2013.
- [74] G.D. Spyropoulos, M. Stylianakis, E. Stratakis, and E. Kymakis. Plasmonic organic photovoltaics doped with metal nanoparticles. *Photonics and Nanostructures - Fundamentals and Applications*, 9(2):184 – 189, 2011. Emerging Trends and Novel Materials in Photonics.
- [75] Anna Loiudice, Aurora Rizzo, Luisa De Marco, Maria R. Belviso, Gianvito Caputo, P. Davide Cozzoli, and Giuseppe Gigli. Organic photovoltaic devices with colloidal TiO₂ nanorods as key functional components. *Physical Chemistry Chemical Physics*, 14:3987–3995, 2012.
- [76] Chen Tao, Shengping Ruan, Xindong Zhang, Guohua Xie, Liang Shen, Xiangzi Kong, Wei Dong, Caixia Liu, and Weiyu Chen. Performance improvement of inverted polymer solar cells with different top electrodes by introducing a MoO₃ buffer layer. *Applied Physics Letters*, 93(19), 2008.
- [77] Fei Huang, Hin-Lap Yip, and Yong Cao, editors. *Polymer Photovoltaics*. Polymer Chemistry Series. The Royal Society of Chemistry, 2015.
- [78] Haiyan Sun, Jonas Weickert, Holger Christian Hesse, and Lukas Schmidt-Mende. UV light protection through TiO₂ blocking layers for inverted organic solar cells. *Solar Energy Materials and Solar Cells*, 95(12):3450 – 3454, 2011.

- [79] Mingjun Wang, Yuan Li, Huihui Huang, Eric D. Peterson, Wanyi Nie, Wei Zhou, Wei Zeng, Wenxiao Huang, Guojia Fang, Nanhai Sun, Xingzhong Zhao, and David L. Carroll. Thickness dependence of the MoO₃ blocking layers on ZnO nanorod-inverted organic photovoltaic devices. *Applied Physics Letters*, 98(10), 2011.